Development of Cell-Based Assays for the Evaluation of novel SARS-CoV-2 Inhibitors

KYRA KLIJMEIJ, BSC – UTRECHT UNIVERSITY

23/05/2022

LAYMAN'S SUMMARY

SARS-CoV-2, the virus responsible for the COVID-19 pandemic, has greatly impacted society. Academia and the drug development industry have been making fast advances to identify drugs against the virus. The efficacy and safety of drugs are often tested in cultured cells before they can be administered to animals or humans. This project aimed to develop two different cell-based assays that can evaluate the potential of new drugs. The assays that were designed in this project can all be performed safely as they do not require a live virus. These assays can also be easily adapted to test drugs targeting other coronaviruses.

The first assay is based on the SARS-CoV-2 Main protease (M^{pro}), a protein that can cut long viral proteins into each active protein that is involved in viral replication. M^{pro} can cut a specific part of an inactive, cyclized reporter protein. Upon linearization, the reporter protein gets activated and releases a luciferase signal. Drugs that inhibit the activity of M^{pro} will therefore prevent the release of a signal. The system has been shown to work, but the luciferase had low activity after activation of M^{pro}. Further optimization is therefore needed.

The second assay is based on the entry pathway of the virus into the cell. The virus can bind to the cell and fuse together to insert its genome and start viral replication. This is done with help of the viral spike-protein that is presented on the membrane of one cell that will bind to a receptor of another cell, causing cell-cell fusion. We established an automated and unbiased method to visualize and quantify the fusion activity based on the fluorescent signal released by the fused cells. Drugs can inhibit fusion and this assay can thus assess the efficacy of the drugs. However, these fusion calculations are not yet accurate and further improvements need to be made. Nevertheless, visually, the prevention of fusion formation after the addition of various drugs can be adequately observed. Measuring the absolute value of the fluorescent signal may be a good alternative to improve quantification.

UTRECHT UNIVERSITY, VIROLOGY DIVISION

ABSTRACT

SARS-CoV-2 has made a large impact on society in the past years due to its high transmissibility which led to the COVID-19 pandemic. Academia and the drug development industry have made fast advances to provide potent inhibitors against the virus, but the holy grail has not yet been found. The potency of these inhibitors can be tested in several assays. Cell-based assays are favourable as, in contrast to biochemical assays, they can assess the cell-permeability and toxicity of the inhibitors. This project, therefore, aimed to develop multiple cell-based assays for the evaluation of potential inhibitors that each target various aspects of the viral replication cycle to advance the discovery of novel and much-needed SARS-CoV-2 inhibitors.

The viral replication can be inhibited by targeting the viral Main Protease (M^{pro}). This protease has been well studied for various coronaviruses and is a popular drug target. A previous assay has been designed around the M^{pro} (Van der Linden et al., 2014; manuscript in preparation) but this assay lacked sensitivity and was not able to detect inhibitors with a lower inhibitory efficacy. A new assay was therefore designed to also identify less potent inhibitors. This assay is based on a cyclic luciferase, that can be linearized after M^{pro} cleavage. Linearization enables luciferase activation and loss of signal can therefore imply successful inhibition. The assay was compared to the previous luciferase assay and showed lower luciferase activity than the previous system. Alterations in transfection time and plasmid DNA concentrations did not improve the activity. Other factors came to light that may influence and improve the assay for future use. Currently, this assay can be easily performed but cannot be used for SARS-CoV-2 inhibitor identification in its current state.

To assess cell entry inhibition, a cell-cell fusion assay was established that can be performed in a BSL-1 setting, as opposed to the BSL-2 setting that is being used for the established pseudotype virus entry assay. SARS-CoV-2 can induce syncytia formation by spike protein-induced membrane fusion. HEK293T cells are transfected with SARS-CoV-2 spike-protein and GFP S(11) and added to VeroE6 cells transfected with TMPRSS2 and GFP S(1-10). Due to GFP complementation after fusion, the fusion activity can be visualized. After upscaling and automation of the imaging and quantification of the assay, the assay can visually detect fusion inhibition by various compounds. The fusion inhibition is currently quantified via algorithmic syncytia identification. This method provides large improvements in the performability of the assay as it is less time-consuming than manual counting and allows for the upscaling of the assay. However, this method is accompanied by measurement inaccuracies that lead to the misidentification of syncytia. More accurate quantification may be provided by measuring GFP intensity.

Even though the assays are still in need of further optimization, they are at this moment easy to perform, can be applied in a BSL1/2 setting, and show promise for successful antiviral identification. The future use of these assays for the identification and evaluation of novel SARS-CoV-2 inhibitors is therefore not yet dismissed.

TABLE OF CONTENTS

LIST OF COMMON ABBREVIATIONS

ACE2	Angiotensin-Converting Enzyme 2	**Nsp**	Non-structural protein
BFP	Blue Fluorescent Protein	**PL^{pro}**	Papain-like protease
BSL	Biosafety Level	**RBD**	Receptor-Binding Domain
COVID-19	Coronavirus disease 2019	**RLuc**	Renilla Luciferase
CycLuc	Cyclic Luciferase	**SARS-CoV-2**	Severe acute respiratory syndrome coronavirus 2
FLuc	Firefly Luciferase	**S-protein**	Spike Protein
FP	Fusion Peptide	**TEV^{pro}**	Tobacco Etch Virus protease
GAL4BD	Gal4 Binding Domain	**TMPRSS2**	Transmembrane protease, serine 2
GFP	Green Fluorescent Protein	**VP16AD**	VP16 Activating Domain
M^{pro}	Main Protease	**WT**	Wild-type

UTRECHT UNIVERSITY, VIROLOGY DIVISION

1 GENERAL INTRODUCTION

Severe acute respiratory syndrome coronavirus 2 (SARS-CoV-2) has made a great impact on society in the past years due to its high transmissibility, leading to hundreds of millions of cases all over the world[1,2]. The illness caused by SARS-CoV-2 was named coronavirus disease 2019 (COVID-19) by the World Health Organization (WHO). Most infected people will develop mild to moderate symptoms such as dry cough, fever, and loss of smell and taste, but in severe cases, some people develop difficulty breathing and chest pain which will require hospitalization[3]. With the first case reported in early December 2019, WHO declared the situation a global pandemic in March 2020 which has resulted in over 6 million deaths[1,2,4].

Due to the development of effective vaccines, COVID-19 morbidity has decreased in the vaccinated population[5]. However, even though it is an important part of the fight against SARS-CoV-2, vaccination is a preventative measure and is unable to cure the infected. New variants have been emerging, of which some are less sensitive to the currently approved vaccines[6]. Therefore, antivirals are needed alongside vaccines to inhibit virus infection and to limit the spread of the virus as well as disease progression.

Traditional development of new compounds takes years. However, the pandemic has forced a more rapid and inventive form of drug development that led to the creative repurposing of previously developed drugs[7]. Various small molecules (e.g. PaxLovid[TM]; mulnupiravir) and monoclonal antibodies (e.g. Regdanvimab; sotrovimab; casirivimab/imdevimab) that work against COVID-19 have already gained market approval by the EMA[7,8].

Potential inhibitors undergo several *in vitro* tests to validate their efficacy and toxicity before they can be subjected to animal experiments. This is often done via biochemical or cell-based assays. Biochemical assays are more homogenous and very specific to the target of interest. However, there is large uncertainty on how the selected compounds will react in a cellular environment[9]. With cell-based assays, we can predict the *in vivo* behaviour of the potential compounds (e.g. efficacy, toxicity, cell permeability), but several other challenges still need to be overcome as they often have problems with automation, predictability, and speed[10]. Moreover, current screening is often performed with live-virus providing unnecessary lab safety issues[11]. This can be circumvented by utilizing only a specific viral protein not the whole virus, thereby reducing the safety level to BSL-2 or -1[12]. Providing well-established cell-based assays with an identified target will aid in characterizing novel antiviral compounds thereby accelerating the drug discovery process.

Several parts of the SARS-CoV-2 replication cycle can be inhibited. The replication cycle of this positive-sense single-stranded enveloped virus begins with the binding of the Spike protein (S-protein) to the cellular receptor ACE2 (Fig. 1)[13]. The virus can enter the cell via two pathways: 1) the cell surface pathway or 2) the endocytic pathway[14]. During the cell surface pathway, the transmembrane protease, serine 2 (TMPRSS2) cleaves the S-protein to fuse the viral and cellular membranes. The S-protein consists of two domains - a receptor-binding domain (S1) and a membrane fusion domain (S2) - and is separated by an S1/S2 cleavage site. A second cleavage site, S2', appears to be the primary target of TMPRSS2, and cleavage of S2' – and potentially also S1/S2 –causes refolding of the S-protein, leading to disassociation of S1 and exposure of the fusion pore. Additionally, the heptad repeat (HR)2 domain of the S-protein folds back and associates with the HR1 domain, bringing the two membranes closer together to initiate membrane fusion[15,16]. The endocytic pathway works similarly but depends on cathepsins – mainly cathepsin L – to induce membrane fusion after endocytosis. The endocytic
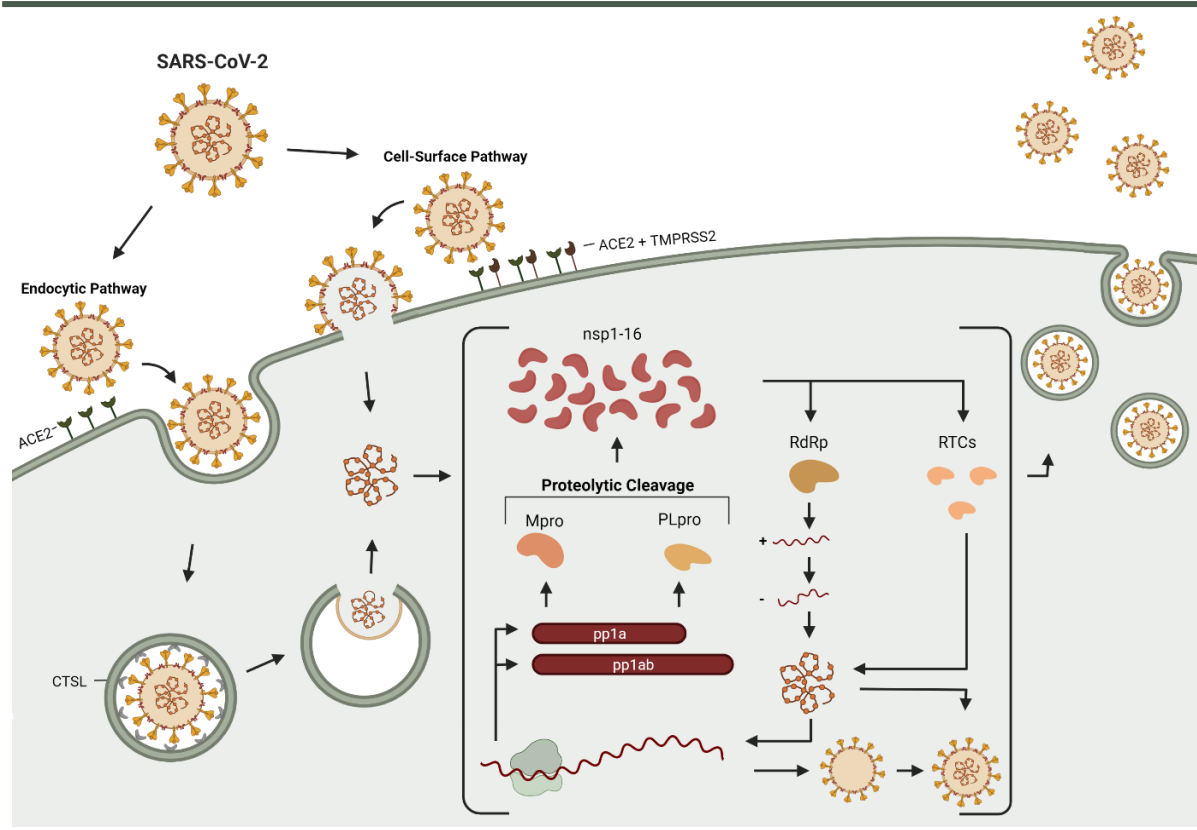
Fig. 1. 1 Schematic representation of the replication cycle of SARS-CoV-2. Entry of SARS-CoV-2 begins with binding to its cellular receptor, ACE2. The virus membrane needs to fuse with the cellular membrane to release its genome to the cytosol via 1) the endocytic pathway or 2) the cell-surface pathway. With the endocytic pathway, the viral particle enters the cell via endocytosis. Host proteases, such as Cathepsin L (CTSL), cleave the S2 portion of the spike protein, exposing the fusion protein, resulting in endosomal membrane fusion and the release of viral RNA in the cytosol. In the case of the cell-surface pathway, serine proteases such as TMPRSS(2) cleave the spike protein directly after ACE2 binding, leading to plasma membrane fusion and viral RNA injection without endocytosis. The viral RNA then attaches to host ribosomes, which translate the polyproteins (pp1a and pp1ab) that release the main protease (M[pro]) and papain-like protease (PL[pro]) via autocleavage. These proteases release 16 non-structural proteins (nsps) responsible for the formation of the Replication and Transcription Complexes (RTCs) that function to process, modify, and proofread newly synthesized viral RNA. Nsp7, -8, and -12 will compose the Replication-dependent RNA polymerase (RdRp) that will help synthesize a positive-sense RNA template for the final negative-sense genome copies. Structural proteins are not present on the polyproteins and are translated separately by host ribosomes. New viral RNA can then be used for further replication purposes or be packaged in progeny viral particles that most likely will secrete from the cell in small secretory vesicles. (Created with BioRender)

pathway is preferred over the cell surface pathway in the absence of TMPRSS2[14]. Blocking the binding and fusion of the viral membrane with the cellular membrane prevents viral entry and is one of the most efficient methods to inhibit viral infection.

Viral replication can be further inhibited by targeting the replication machinery. After the membrane fusion, the viral RNA is released into the cytosol. The translation of two major polyproteins (pp1a and pp1b) occurs upon the attachment of the viral RNA to the host ribosome[17,18]. These polyproteins are processed into individual viral proteins by two viral proteases, papain-like protease (PL[pro]; a.k.a. nsp3) and main protease (M[pro]; a.k.a. nsp5), releasing non-structural proteins (nsp) 1-3 and nsp4-16 respectively[18]. Especially the M[pro] has been a popular drug target for SARS-CoV-2. This homodimeric cysteine protease cleaves the polyproteins predominantly after the amino acid sequences Leu-Gln↓Ser-Ala-Gly and contains three domains[19,20]. Domain I and II harbour the active site, whilst domain III serves a stabilizing purpose[19]. Viral RNA replication further depends on the RNA-dependent RNA polymerase (RdRp) which comprises a catalytic subunit nsp12 as well as two accessory subunits,

nsp7 and nsp 8. Newly synthesized RNAs can either enter another round of replication or be packaged into newly formed virions and exit the cell in small secretory vesicles[13,17,21–23].

Several stages of the SARS-CoV-2 replication cycle can be targeted when developing or repurposing compounds inhibiting SARS-CoV-2. Cell entry can be inhibited by targeting the S-protein, ACE2, TMPRSS2, or other host proteases involved in cell entry. In addition, targeting viral proteins or proteases such as M^{pro}, PL^{pro}, or RdRp can limit viral replication.

In this study, we aimed to develop dedicated cell-based assays that can be utilized to identify novel SARS-CoV-2 inhibitors and to reveal the mode-of-action of potential compounds. Among all the various potential antiviral targets, we have chosen to focus on the viral protease M^{pro} and the membrane fusion event during viral entry.

2 RESULTS AND DISCUSSION

2.1 CELL-BASED MPRO ASSAY

The Main Protease (also referred to as 3CL[pro] or nsp 5) of SARS-CoV-2 shares 78% to 96% similarity with SARS-CoV M[pro] and plays an important role in viral replication[19,20,2420,25] M[pro] is currently one of the best-characterized drug targets for SARS-CoV-2 and has therefore been widely studied in the past year[20], yielding several inhibitors which could successfully inhibit *in vitro* and *in vivo* viral replication[26].

In this lab, a cell-based M[pro] dual-luciferase assay was developed which is derived from the previously established enterovirus 3Cpro assay (referred as to the G5Luc system; Fig. 2.1.1) (manuscript in preparation)[27]. It could identify several potential anti-M[pro] compounds. Yet, due to a stringent threshold, potential drug hits that may be transformed into potent inhibitors could not be detected. This project, therefore, aimed to develop a cell-based cyclic-luciferase assay that can evaluate inhibitor efficiency with higher sensitivity.

Establishment and optimization of M[pro] CycLuc reporter assay

We designed a new cell-based M[pro] assay based on a cyclic *Firefly* luciferase (CycLuc) reporter system for Tobacco Etch Virus (TEV) protease[28]. This CycLuc consists of the N-terminal part and C-terminal part of *Firefly* luciferase (FLuc) which are divided by the TEV cleavage site. FLuc can be activated by conformational change after cleavage by TEV[pro]. This cleavage site for TEV[pro] has been replaced with a M[pro] cleavage site by site-directed mutagenesis and the resulting construct is named a M[pro] CycLuc reporter (Fig. 2.1.1).

The CycLuc system was first tested in a proof-of-concept study. HEK293T cells were co-transfected with the *Firefly* luciferase (pcDNA3_cycluc_Mpro) and pBIND_Mpro_VP16 containing WT or C145A M[pro] and a *Renilla* luciferase (RLuc) to measure the transfection efficiency. The catalytically inactive mutant of M[pro] (C145A) was included as a negative control[29–31]. The FLuc was normalized to RLuc activity. The CycLuc system was directly compared to the previously established G5Luc system using the same conditions for each assay (Fig. 2.1.1). The RLuc levels were similar across both systems, with a slight increase in activity for the C145A M[pro] CycLuc Luciferase condition (Fig. S1.1A). As expected, there was an increase in FLuc/RLuc activity for the C145A M[pro] condition compared to WT M[pro] for G5Luc (Fig. 2.1.2A; S1.1A). However, no difference in the absolute FLuc activity was observed between WT and C145A M[pro] for CycLuc (Fig. S1.1A). Yet, a minor increase in luciferase activity for the WT M[pro] condition was seen after normalization to RLuc (Fig. 2.1.2A).

To assess whether the expression level of CycLuc may have impacted the luciferase activity, various concentrations – ranging from 50 to 200 ng of – of M[pro] pCycLuc were added to the HEK293T cells. Again a notable increase in RLuc activity could be observed after the addition of C145A M[pro] for all plasmid concentrations (Fig. S1.1C). No clear differences in FLuc activity between WT and C145A M[pro] were seen (Fig. S1.1C). After normalization, no clear concentration-dependent activity of CycLuc could be observed (Fig.2.1.2B).

Next, the transfection time was increased to 48h and 72h as this could maybe lead to increased expression of the CycLuc protein. Similar to before, the RLuc activity was increased for C145A M[pro] and no notable difference in FLuc activity between conditions could be observed (Fig. S1.1B). The FLuc/RLuc activity was comparable between transfection time conditions (Fig.2.1.2C). Even though the difference is small, CycLuc activity can be increased after the addition of WT M[pro]. Yet, it does not seem to be dependent on transfection time or plasmid concentration.

pBIND-M^pro(SARS2)-VP16
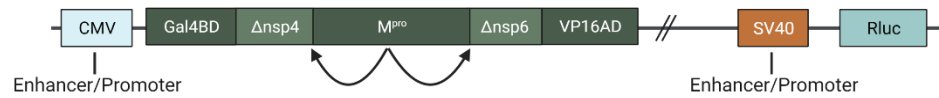
G5Luc
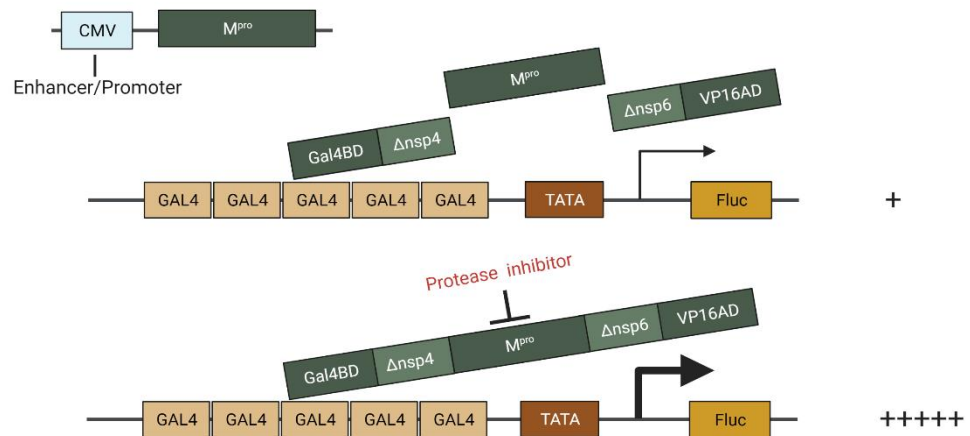
CycLuc
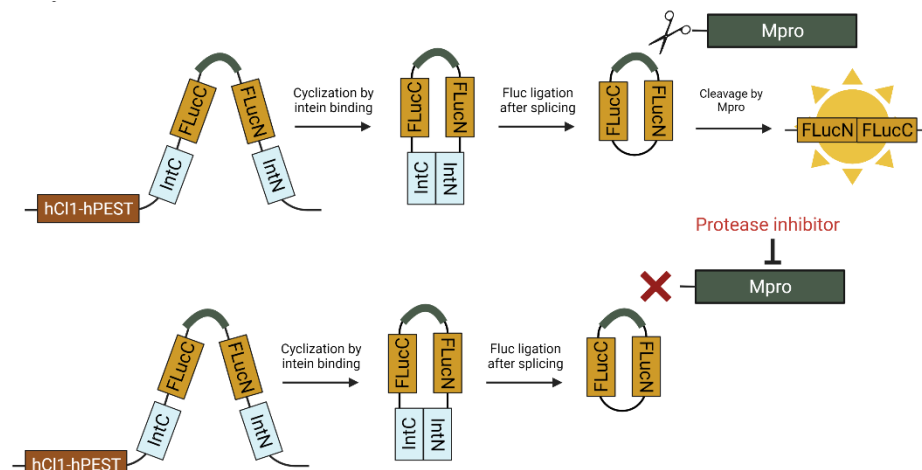
Figure 2.1. 1 - Mechanism behind the Mpro luciferase assays. A) G5Luc assay adapted from *Van der Linden et al., 2014* (manuscript in preparation). M^pro cleaves the M^pro construct at the inserted neighbouring M^pro cleavage sites (nsp4/nsp6), inhibiting luciferase (FLuc) activation. Prevention of M^pro cleavage by protease inhibitors will result in increased activation of the luciferase. B) The cyclized luciferase construct was adapted to contain a *Mpro* cleavage site. The C- and N-terminal of the inteins of the CycLuc sequence will bind, cyclize the luciferase, and will subsequently be spliced off. The remaining protein will contain the N- and C-terminal of the Firefly Luciferase that are cyclized by the *Mpro* cleavage site, and therefore not able to produce a luciferase signal. An hCl1-hPEST sequence ensures degradation of uncyclized luciferase. Cleavage by *Mpro* will result in linearization and thereby the active form of the protein, leading to correct and efficient expression of the firefly luciferase. (Created with BioRender)

Validation of CycLuc M^pro expression

Since neither increasing pCycLuc concentration nor prolonged incubation time affected the expression level of FLuc, we questioned whether CycLuc is expressed at all. As we adapted the CycLuc system from a TEV^pro CycLuc, we performed the assay using the TEV CycLuc to assess whether higher luciferase activity could be achieved with this protein. We co-transfected the cells with pCycluc (TEV) and TEV^pro expressing plasmid (pcDNA_RFP-TEVprotease) and measured the FLuc activity. To obtain the most optimal condition, different concentration ratios were tested. RFP activity was visualized after 24h and 48h post-transfection showing clear signs of expression after both timeframes (Fig. S1.2A, B). The ratio of 100/70 ng (CycLuc/protease) showed the highest overall FLuc activity as well as the largest difference between mutant- and WT-induced FLuc activity (Fig. S1.2B). This ratio was therefore further used to directly compare the FLuc activity of M^pro CycLuc with the original TEV CycLuc. However, the transfection efficiency had a large impact on M^pro CycLuc activity as the RLuc activity of the C145A M^pro variant was – again – considerably larger than its WT counterpart (Fig. 2.1.2D, Fig S1.2C). Therefore, the two cyclic luciferases could not be accurately compared without a form of normalization. As the TEV^pro plasmid does not contain RLuc, no normalization could be performed.

Even though for M^pro CycLuc the normalized luciferase activity was low after each applied condition, a clear difference in activity between the C145A or WT M^pro conditions could be observed. Moreover, M^pro CycLuc activity remained reasonably consistent throughout all performed assays staying <1 (FLuc/RLuc) after WT M^pro activation. To see whether low expression levels are the cause behind the relatively low luciferase activity, western blotting and immunofluorescence assays were performed.

The low activity of CycLuc compared to G5Luc raised questions about the expression of the CycLuc plasmid in the HEK293T cells. This was therefore assessed by western blotting and immunofluorescence assays (IFA). By targeting the HIS-tag on the M^pro CycLuc and TEV CycLuc plasmids with an anti-HIS antibody, the expression of the cyclic luciferases can be visualized. His-OSBP was taken along as a positive control.

The IFA was performed in HeLa cells and was visualized after three different transfection times (24h, 48h, and 72h). Results showed little difference in fluorescent activity between transfected and non-transfected cells (Fig. 2.1.3A). Increasing transfection time seemed to show small hints of expression for M^pro CycLuc, mostly after 72h. These hints of expression could also be seen for both CycLucs after 48h. However, these results were very similar to the negative control. Moreover, the OSBP control – only tested at 24h – was weakly/not expressed. Therefore, as the controls were inaccurate, no reliable conclusion can be drawn from the IFA results. More experiments on CycLuc expression were performed with western blotting.

The western blotting was first performed with 1000 ng plasmid DNA with cell harvesting after 24h post-transfection. The results showed a clear band at the expected size for the OSBP control (~92kD), but both M^pro and TEV CycLuc (~80kD) could not be detected (Fig. 2.1.3B). The experiment was therefore repeated using two CycLuc concentrations (1000 ng and 2500 ng) and three different transfection times (24h, 48h, 72h) to see whether plasmid DNA concentration and transfection time impact the expression of the cyclic luciferases (Fig.2.1.3C). The results were similar to before as no bands were visible at the expected size.

The results from the IFA and western blots imply that there is no or low expression of the M^pro and TEV CycLucs. However, this is contradictory to the results from the luciferase assays as a small increase in luciferase activity could be observed after protease cleavage and TEV CycLuc expression was visible using the mCherry tag. This indicates that the luciferase proteins were present and successfully expressed, but could not be detected via the attached HIS-tag.
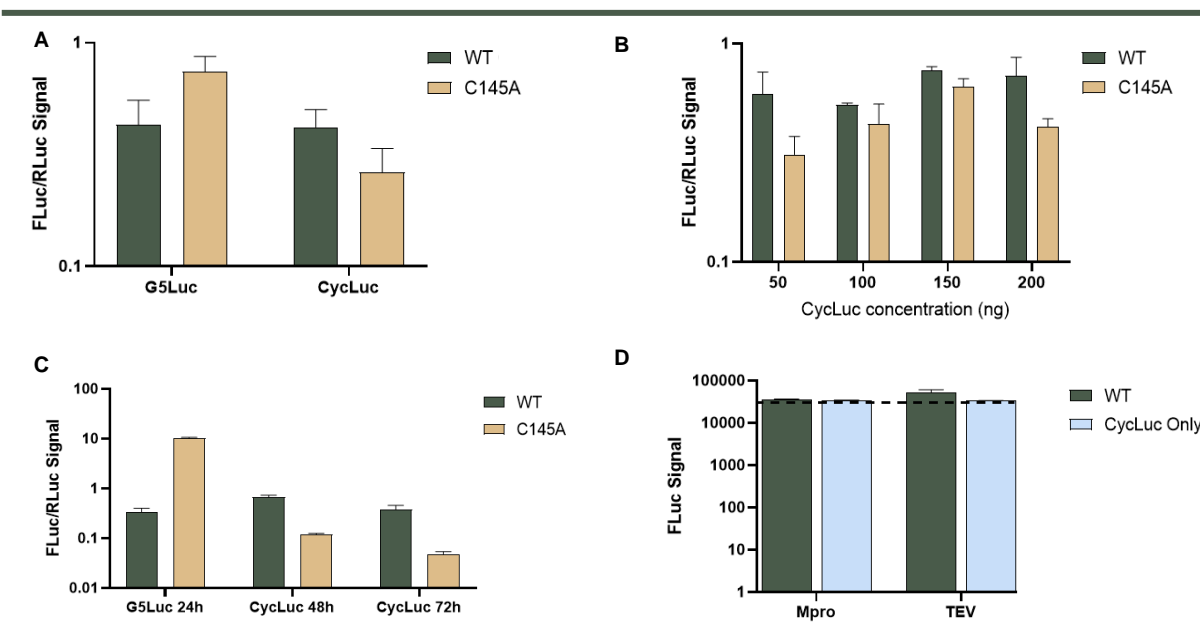
Figure 2.1.2– Proof-of-concept cyclic luciferase (CycLuc) assays. HEK293T cells were co-transfected with cyclic luciferase and WT or C145A (inactive) mutant M^{pro}. *Firefly* (FLuc) and *Renilla* (RLuc) luciferase activity were visualized with the GloMax® Explorer using the Dual-Luciferase® Reporter Assay System. A) Firefly luciferase (FLuc) activity of CycLuc and G5Luc after co-transfection with wild-type (WT) or mutant (C145A) M^{pro}. Normalized for transfection efficiency with Renilla Luciferase (RLuc) activity (FLuc/RLuc) B) Effect of various pCycLuc concentrations on luciferase activity for WT and C145A M^{pro}. Normalized for transfection efficiency with Renilla Luciferase (RLuc) activity (FLuc/RLuc) C) Luciferase activity for CycLuc 48h and 72h post-transfection. G5Luc activity 24h post-transfection is added as a positive control. Normalized for transfection efficiency with RLuc activity (FLuc/RLuc) D) Firefly Luciferase (FLuc) activity for M^{pro} and TEV CycLuc after the addition of the respective proteases. As a control, the CycLucs are transfected without the proteases (CycLuc Only). Background luminescence is illustrated with the dotted line.
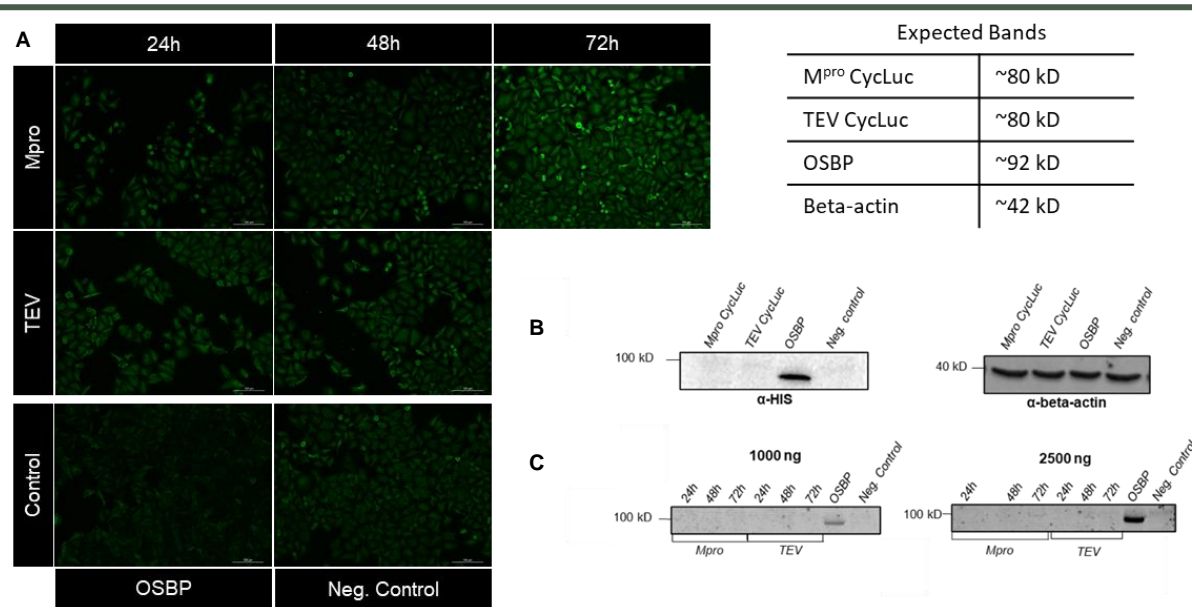
Figure 2.1. 3– Visualization of Mpro CycLuc expression. Mpro CycLuc has an expected size of ~80 kD. Positive controls are TEV CycLuc (~80 kD) and OSBP (~92 kD). The negative control are non-transfected cells. A) Immunofluorescence assay with varying transfection periods of 24h, 48h, and 72h. HeLa cells were transfected with pcDNA3_Cycluc_TEVS, pcDNA3_Cycluc_Mpro, or HIS-OSBP and stained with anti-HIS antibody and 488 Goat Anti Mouse after 24h, 48h, and 72h. OSBP was only transfected for 24h. B, C) HEK293T cells were transfected with pcDNA3_Cycluc_TEVS, pcDNA3_Cycluc_Mpro, or HIS-OSBP and chemically lysed the following day. The proteins were separated with SDS-PAGE and stained with anti-HIS antibody for CycLuc and OSBP detection. Samples were reblotted with beta-actin (~42 kD) to assess whether the western blotting was performed successfully. After the primary western blot (B), samples containing variations in transfection time and plasmid DNA concentrations were used to detect differences in protein production (C).

Discussion

Cyclic luciferase reporter systems have previously been established for monitoring the activity of caspase-3 and TEV protease [28,32]. In this project, we aimed to develop a CycLuc reporter assay for SARS-CoV-2 M[pro] activity which can potentially be used as a screening platform for finding a potential inhibitor. We took the CycLuc reporter for TEV[pro] and modified the cleavage site to M[pro]-specific one, but we could not validate this system due to the limited activity of CycLuc-M[pro] (Fig. 2.1.2). This poor sensitivity was believed to be due to low protein expression as CycLuc could not be detected via its HIS-tag (Fig.2.1.3). However, the HIS-tag is placed before the hCL1-hPEST degradation sequence that is included to reduce the influence of uncyclized luciferases. After cyclization, this hCl1-hPEST sequence and thus most likely the HIS-tag are removed. There may therefore be sufficient expression of CycLuc, but this could not be visualized due to the removal of the HIS-tag. Placing a second tag after the hCl1-hPEST sequence may allow for the detection of the cyclized protein and therefore give a better indication of the expression level of CycLuc.

During the proof-of-concept experiments, M[pro] was able to activate luciferase expression (Fig. 2.1.2). However, the luciferase activity did not reach similar levels as with the previously constructed G5Luc assay. Moreover, only a small decrease in activity could be noted after the addition of the mutant C145A M[pro] compared to WT M[pro]. This leaves only a narrow range for potential M[pro] inhibition, making it difficult to distinguish between the inhibition potencies of each inhibitor.

While we were working on this project, a similar cell-based cyclic luciferase assay for the SARS-CoV-2 M[pro] was reported by others that was also inspired by the CycLuc-TEV[pro] reporter system[28,33]. Unlike our system, it could be used for screening potential protease inhibitors. Although we took a similar approach, there were several differences in the setting of each assay: 1) An alternative cleavage site had been chosen for M[pro] digestion (TVRLQ↓A (nsp9-10) instead of our VARLQ↓SGF). As M[pro] can have clear preferences for residues per cleavage site position, choosing the most attractive cleavage site is of high importance[34]. M[pro] has shown to have a great affinity for both sequences[35]. 2) A stable Huh7.5 CycLuc+ cell line was developed for a more constant expression of CycLuc, removing potential variations in expression per condition. Moreover, this enables the delayed addition of M[pro], ensuring luciferase cyclization before cleavage. Differences in activity after the addition of M[pro] were seen depending on cell types, implying that cell type can also play a role in luciferase activity. HEK293T cells were not included there and it is therefore not known how this cell type would behave in their experiment. Nevertheless, it might be profitable to perform the assay with their most successful cell line, namely Huh7.5 cells. 3) For the main experiment, cells were infected with SARS-CoV-2. A complication with this method is that the assay must be performed at BSL-3, reducing the safety and practicality of the assay. As our assay uses M[pro] alone, this problem is circumvented. However, it must be noted that the M[pro] used for this assay was embedded in a construct containing neighbouring cleavage sites as well as a part of nsp3 and nsp6 proteins, which may have interfered with the assay.

With the M[pro] cyclic luciferase assay, we were able to detect a visible increase in luciferase activity in the presence of WT M[pro]. The luciferase activity does need to be increased as currently it cannot be used for the identification of M[pro] inhibitors. Placing a new tag on the cyclized protein may provide more information regarding the expression of CycLuc. Moreover, the assay may be optimized by adjusting the cell type, the cleavage site, and delaying the addition of M[pro] to ensure full cyclization of the luciferases. All in all, this assay shows promise for future use but needs to be optimized before it can properly detect novel M[pro] inhibitors.

UTRECHT UNIVERSITY, VIROLOGY DIVISION

2.2   Cell–cell fusion assay

SARS-CoV-2 can induce cell-cell fusion[36], which allows the virus to enter neighbouring cells without producing cell-free virus[37]. The neighbouring cells will fuse and these fused multinucleated cells are referred to as syncytia and are a part of the COVID pathology due to their tissue-damaging abilities[37]. The spike protein (S-protein) is responsible for this event. It is expressed on the surface of infected cells and can induce membrane fusion after proteolytic cleavage by host proteases such as TMPRSS2 and furin[36]. Fusion is dependent on the presence of proteases and Ace2 receptors and specific sites of the S-protein, such as the S1/S2 and `S2 cleavage sites[36].

A cell-cell fusion assay utilizes this phenomenon to screen for various types of antiviral compounds. For example, inhibition of the S-protein, TMPRSS2, and ACE2 are all expected to lead to reduced fusion activity and these cell-cell fusion assays can therefore be employed to measure the efficacy of these inhibitors when using the right methodology. This project has adapted a GFP-complementation fusion assay to visualize and quantify syncytia formation[36]. This assay was used to assess the role of the S1/S2 cleavage site on fusion activity and may be well-suited for antiviral screening as fusion inhibition is expected to lead to decreased GFP complementation. Adapting this assay to incorporate fusion inhibition may therefore lead to a strong, quantifiable assay to identify new inhibitors targeting the SARS-CoV-2 entry pathway.

The assay was performed with HEK293T cells transfected with SARS-CoV-2 S-protein, BFP (containing a nuclear localization signal), and GFP subunit (S) 11. Additionally, VeroE6 cells transfected TMPRSS2 and GFPS(1-10) were used and added to the HEK293T cells to initiate fusion formation (Fig. 2.2.1). Multiple HEK293T/VeroE6 cell ratios were tested as this may impact fusion activity and an optimal ratio has not been previously determined[36].

The assay was easily reproducible in our hands but needed more optimization. We further optimized the assay and automated the imaging and quantification procedures. Moreover, we tested several inhibitors to assess whether this assay is suitable for inhibitor identification and quantification of the inhibition efficacy.

Establishment and validation of the experimental condition

The assay was first reproduced on 12 mm coverslips. The syncytia were imaged with a conventional fluorescent microscope (Olympus BX60 WF) and the BFP+ nuclei were counted. The number of nuclei per syncytium and the total number of nuclei per condition represent the size and number of syncytia, respectively. Both VeroE6 and VeroE6 cells overexpressing TMPRSS2 (Vero E6 TMPRSS2+) were used together with HEK293T cells in different ratios (1:10; 1:20; 1:40; 1:80) to establish the condition in which syncytia formation was most optimal.

The highest fusion activity was observed for the 1:10 and 1:20 ratios, particularly for the VeroE6 cells with TMPRSS2 overexpression (TMPRSS2+) (Fig. 2.2.2A, B). These conditions resulted in higher median numbers of nuclei per syncytia (+/- 40 nuclei) and total amounts of nuclei per condition (+/- 400 nuclei) compared to the 1:40 and 1:80 ratios (0-10 nuclei per syncytium; 0-100 total number of nuclei) (Fig.2.2.2A). Several syncytia did not contain BFP+ nuclei, influencing the overall median (see Fig. 2.2.2.B: VeroE6 1:20). Overall, TMPRSS2+ cells showed more nuclei per syncytium (syncytium size) as well as a larger total number (syncytia number), indicating that these cells initiate the formation of more and larger syncytia compared to VeroE6 cells without overexpression of TMPRSS2. Additionally, the addition of more HEK293T cells increased fusion activity, implying that the S-protein, not the Ace2 receptor, should be present in abundance to create higher cell-cell fusion levels. As high levels of fusion could be created, further experiments were performed to test whether the fusion could be
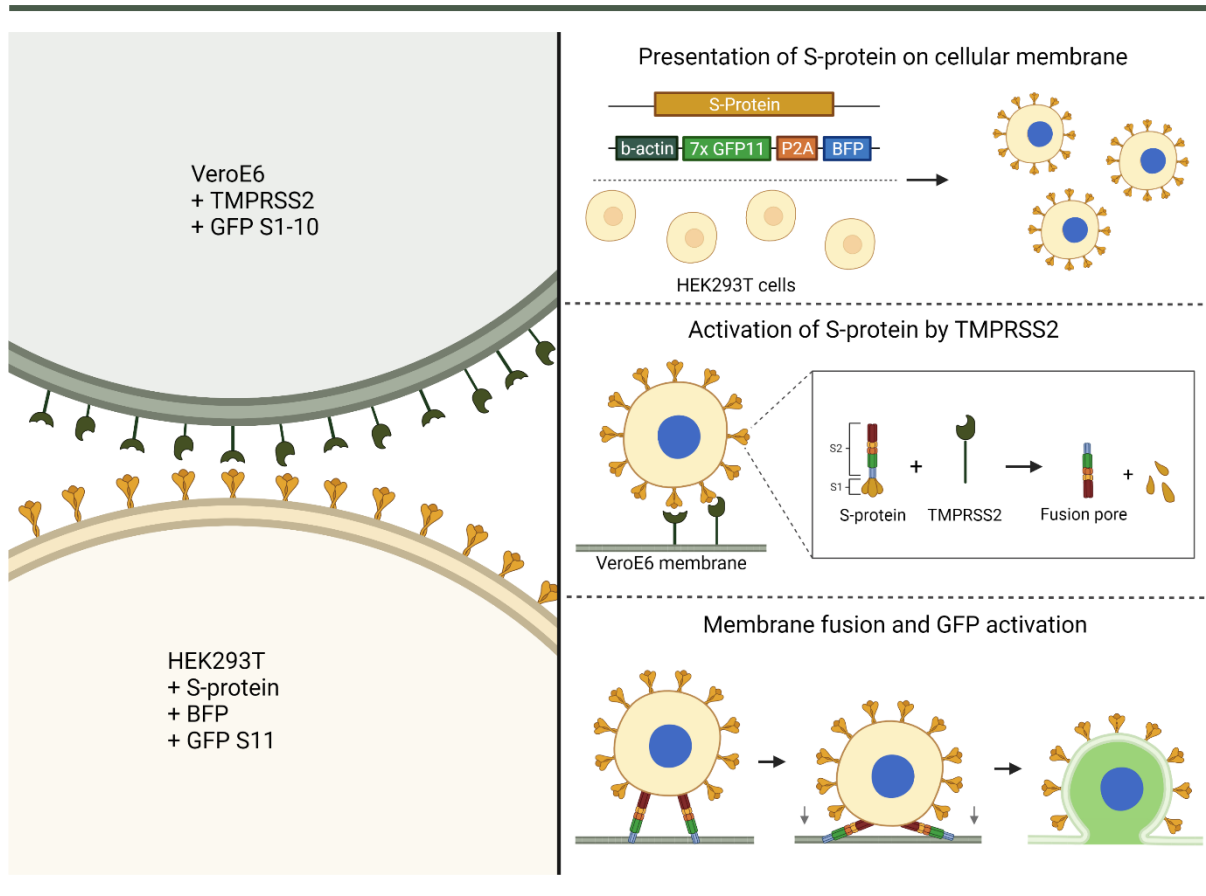
Figure 2.2. 1 – **Schematic representation of the GFP-complementation fusion assay**[39]. After the presentation of the S-protein on the cellular membrane of HEK293T cells (overexpressed with S-protein, BFP, and GFP subunit (S) 11), HEK293T cells will bind to the ACE2 receptor of the VeroE6 cells that are stably transfected with GFP S(1-10) (and TMPRSS2+). The S-protein will be activated after binding, which can be assisted by TMPRSS2, due to S2 site cleavage that leads to exposure of the fusion pore. The fusion pore will insert into the cellular membrane of the target cells (VeroE6), causing membrane fusion and therefore complementation of the GFP subunits. Fused cells will express complete GFP and release a fluorescent signal. Fusion can then be visualized with imaging and the GFP and BFP signalling can be used for the quantification of fusion activity by either measuring GFP+ pixels or counting the BFP+ nuclei. (Created with BioRender)

adequately inhibited using the 1:10 and 1:20 ratios in the VeroE6 and VeroE6 TMPRSS2+ cells using a well-characterized neutralizing monoclonal antibody, REGN#10933 (a.k.a. casirivimab)[38].

For these inhibition assays, REGN#10933 was pre-incubated with S-protein expressing HEK293T cells. Next, the cell-antibody mixture was added to the VeroE6 cells in 1:10 or 1:20 ratios. The fusion activity was imaged and quantified as it was described above. Inhibition with REGN#10933 led to a substantial decrease in syncytia formation (Fig. 2.2.2C, D) visually and quantitively. Both total nuclei count and the number of nuclei per syncytium were greatly reduced in both Vero E6 and Vero E6 TMPRSS2+ cells. Reductions as large as +/- 20 nuclei per syncytium and 474 nuclei in total nuclei count could be observed after addition of the inhibitor. VeroE6 TMPRSS2+ cells showed considerably more fusion and produced a larger difference between wells with and without added antibody than the cells without TMPRSS2 overexpression. The difference between the two ratios for the VeroE6 TMPRSS2+ cells was again nihil with only a difference of 3 nuclei for the median number of nuclei per syncytia (+/- 32 (1:10); +/- 29 (1:20)). In conclusion, Vero E6 TMPRSS2+ cells and adding HEK293T cells in a 1:10 ratio was determined as the most optimal condition. Inhibition could be well-visualized and quantified in this format, indicating that this assay is suitable for the identification of new inhibitors.
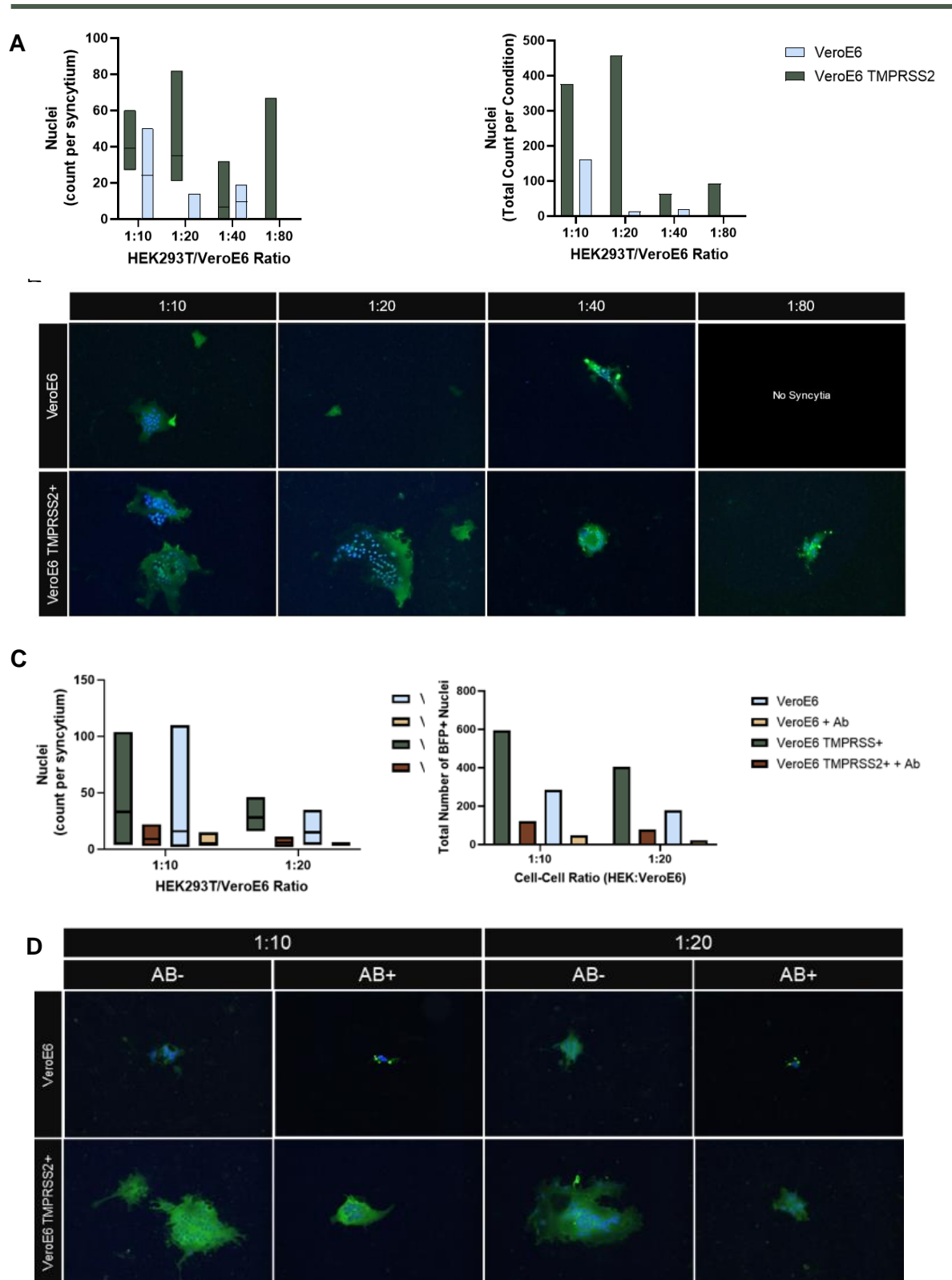
Figure 2.2.2 Optimization of HEK293T/VeroE6 cell ratio. A) Nuclei counts per syncytium (left) and total count per condition (right) for VeroE6 and VeroE6 TMPRSS2+ cells. Count per syncytium is visualized with the min and max number of nuclei in a syncytium. The median is indicated by a black line. B) Representative image (out of 6) per condition taken with Olympus BX60 WF microscope (20x magnification). Syncytia are visualized by reconstituted GFP and BFP-nuclei. C) Fusion inhibition by REGN#10933 (12 µg/well) (+ ab) depicted in nuclei count per syncytia (left) and total nuclei count (right). D) Representative image (out of 6) per condition taken with Olympus BX60 WF microscope (20x magnification). Syncytia are visualized by GFP and HEK293T nuclei are illuminated by BFP. (AB- = without antibody; AB+ = with antibody)

Automation of imaging and quantification procedure

Although we showed that this assay can be used for identifying potential fusion inhibitors, the experimental setup was not yet suitable for the screening of multiple compounds. Only a limited area of the coverslips could be imaged (+/- 25%), which may have resulted in selection bias. Moreover, even though the quantification of the nuclei provided a straightforward indication of the quantity and size of syncytia, this method often showed high variation among values and the counting was laborious and time-consuming.

To overcome these issues, we have employed an 18-well microslide (iBidi). As these slides have a standard format, an automated imaging protocol could be established with the Nikon A1R microscope. This new protocol enabled the imaging of around 80% of the well which led to reduced selection bias and faster imaging. For further automation of the image analysis step, the number of syncytia/well and syncytia size were selected as new measurement points. We build a script using CellProfiler software that was able to identify individual syncytia based on fluorescent activity and estimate the size (area) of each syncytium with adequate accuracy (Fig.S2.2; S2. Raw Data). To accommodate for the large data output, RStudio was used to provide the necessary calculations and graphical visualization of the experiment outcomes (S2. Raw Data). To confirm that the area and number of nuclei of syncytia were interchangeable as measurement points, both factors were measured for several syncytia and a linear correlation between the area and number of nuclei of a syncytium could be observed (Fig. S2.3). The area is accompanied by a large standard deviation, comparable to the number of nuclei per syncytia (see Fig.2.2.2A and C), signifying the large variations between syncytia per condition. Overall, implementing the new imaging and measurement techniques resulted in an increased number of data points, less selection bias, and made the assay less laborious and time-consuming.

During the optimization steps, it came to light that the VeroE6 cell numbers after the incubation period were inconsistent between repeating experiments. With the previously determined ratios, a higher number of VeroE6 cells after incubation leads to the addition of higher numbers of HEK293T cells and therefore inconsistent fusion activity. Therefore, we added a set number of HEK293T cells (4000; 6000;
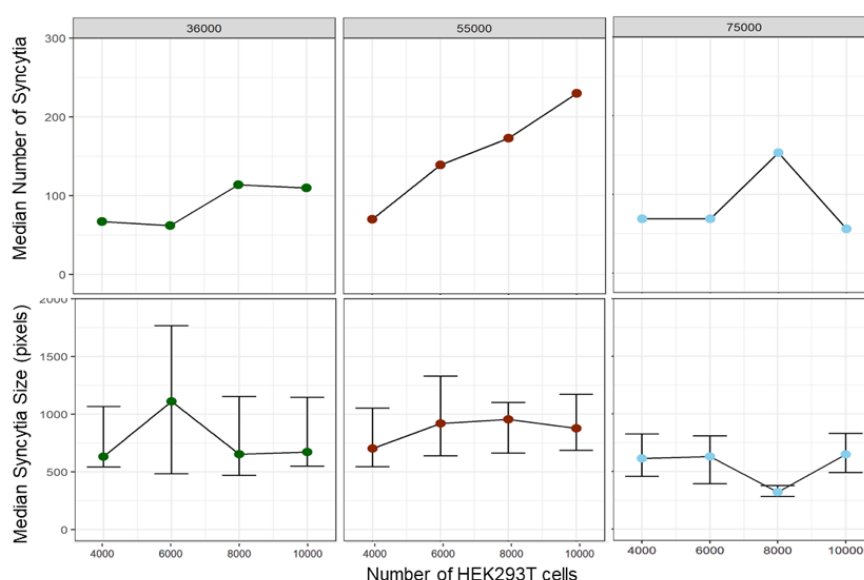
Figure 2.2.3 – Determination of HEK293T/VeroE6 cell numbers to stabilize fusion activity in a 18-well iBidi microslide. Fusion activity for several combinations of HEK293T (4000/6000/8000/1000) and VeroE6 cells (36000/55000/75000) was measured. The VeroE6 cells were plated in a single iBidi microslide and incubated for a day before the HEK293T (+S-protein) cells were added. To allow for sufficient fusion activity, the cells were left overnight at 37°C. Imaging was then performed with NIKON A1R and analysed with CellProfiler software. Data was processed in RStudio.

8000; 10 000) to several amounts of VeroE6 cells (36 000; 55 000; 75 000) to see if there was a correlation between HEK293T and VeroE6 cell number and fusion activity and to check whether we can create a more stable and reliable amount of fusion activity. Adding 4000 HEK293T cells resulted in a similar level of fusion (number: ~75 syncytia per well; size: ~600 pixels per syncytia) regardless of the amount of VeroE6 cells (Fig. 2.2.3). This experiment was repeated on the coverslips, resulting in similar results for the lowest number of HEK293T cells (Fig S.2.1). This confirms that the newly implemented imaging and measuring techniques (i.e. automated imaging, CellProfiler software, set number of cells) also works well in a different format. As the lowest number of HEK293T cells resulted in the most stable fusion in both formats, the 4000/36000 (HEK293T: VeroE6) condition was chosen for future experiments.
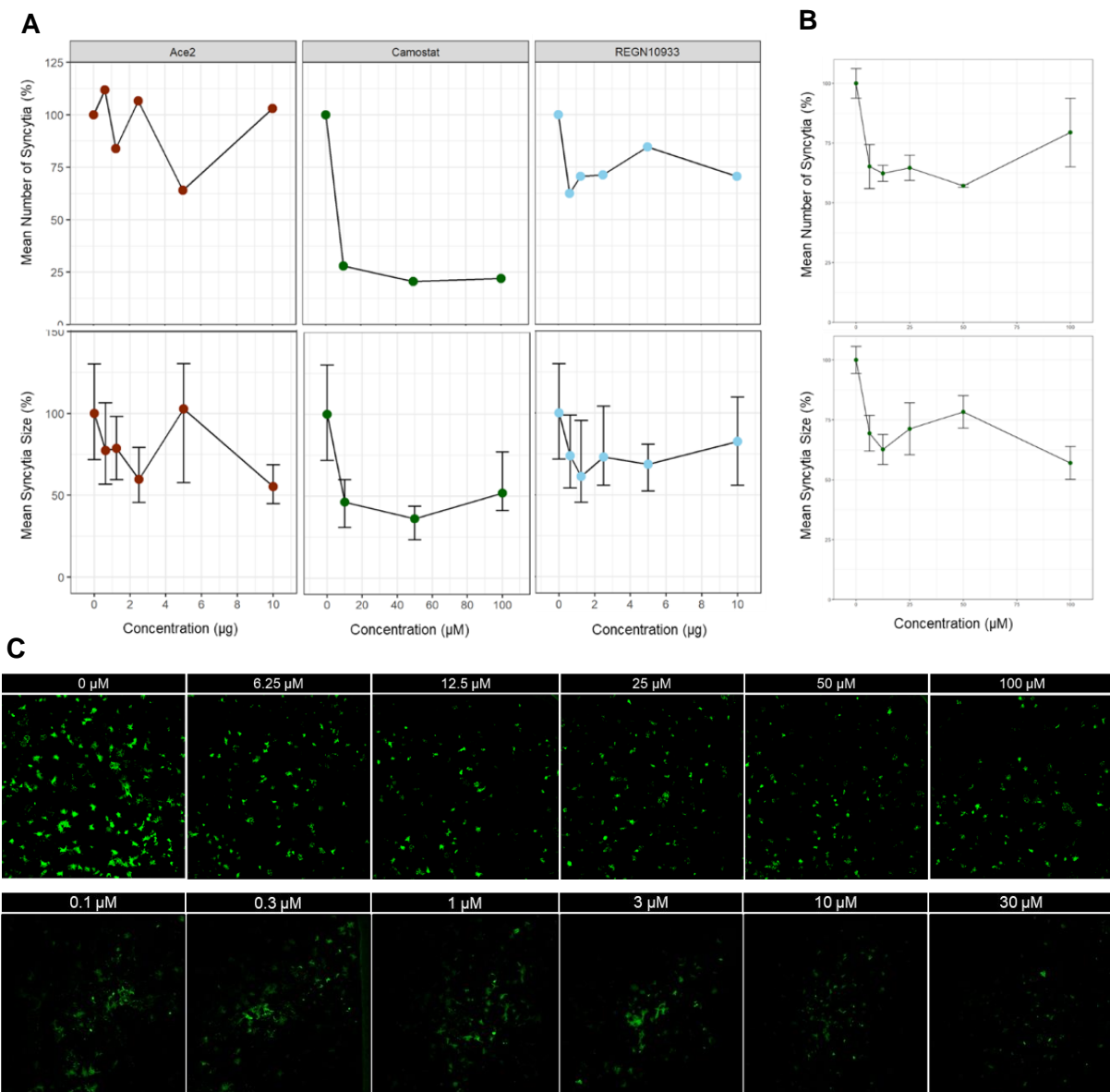
Figure 2.2. 3 – Effect of Ace2, S-protein, and TMPRSS2 inhibition on fusion activity. A) Median number of Syncytia and median syncytia size after inhibition by hACE2, REGN#10933, and camostat. 100% value is derived from the negative control without inhibitory compounds. The assay was performed on 12mm coverslips. B) Concentration range for camostat-induced inhibition (performed in triplicate) on iBidi microslides, measuring the mean number of syncytia and mean syncytia size. The means are calculated from the median numbers from each replicate. Inhibition stabilizes at 60% after addition of the lowest included concentration (6.25 μM). C) A representative microscopic images of the camostat concentration ranges from 0-100 μM (see B for graphical representation) and a second range from 0.1-10 μM (graph not depicted) . Images were taken with the NIKON A1R microscope and analysed with CellProfiler and data was further processed with RStudio.

Fusion inhibition by known anti-SARS-CoV-2 molecules can be visualized and quantified.
The fusion inhibition in the new assay format was assessed by soluble biotinylated hACE2 (scavenging Spike), REGN#10933 (neutralizing antibody), and camostat (TMPRSS2 inhibitor), thereby targeting three different factors involved in cell-cell fusion. These inhibitors were tested using several concentrations and compared to a negative control (no inhibitor). The mean number of syncytia and the mean syncytia size found in this negative control were set at 100%. A decrease up to 40%, 40%, and 75% in the number of syncytia and a reduction up to 45%, 40%, and 60% in syncytia size could be found after the addition of hACE2, REGN#10933, and camostat respectively (Fig. 2.2.4A). The TMPRSS2 inhibitor camostat acted superiorly in comparison to the antibodies that acted on spike/ACE2 binding. The difference in fusion activity between compounds could be well-observed with only a little fusion activity after the addition of high camostat concentrations (Fig. S2.4). As camostat was most efficient in reducing fusion activity, a new range of concentrations was performed to collect more information on the behaviour of the inhibitor in our assay. Camostat showed again a steep decrease in syncytia formation and fusion inhibition stabilized at approximately 40% compared to the uninhibited sample

A

B
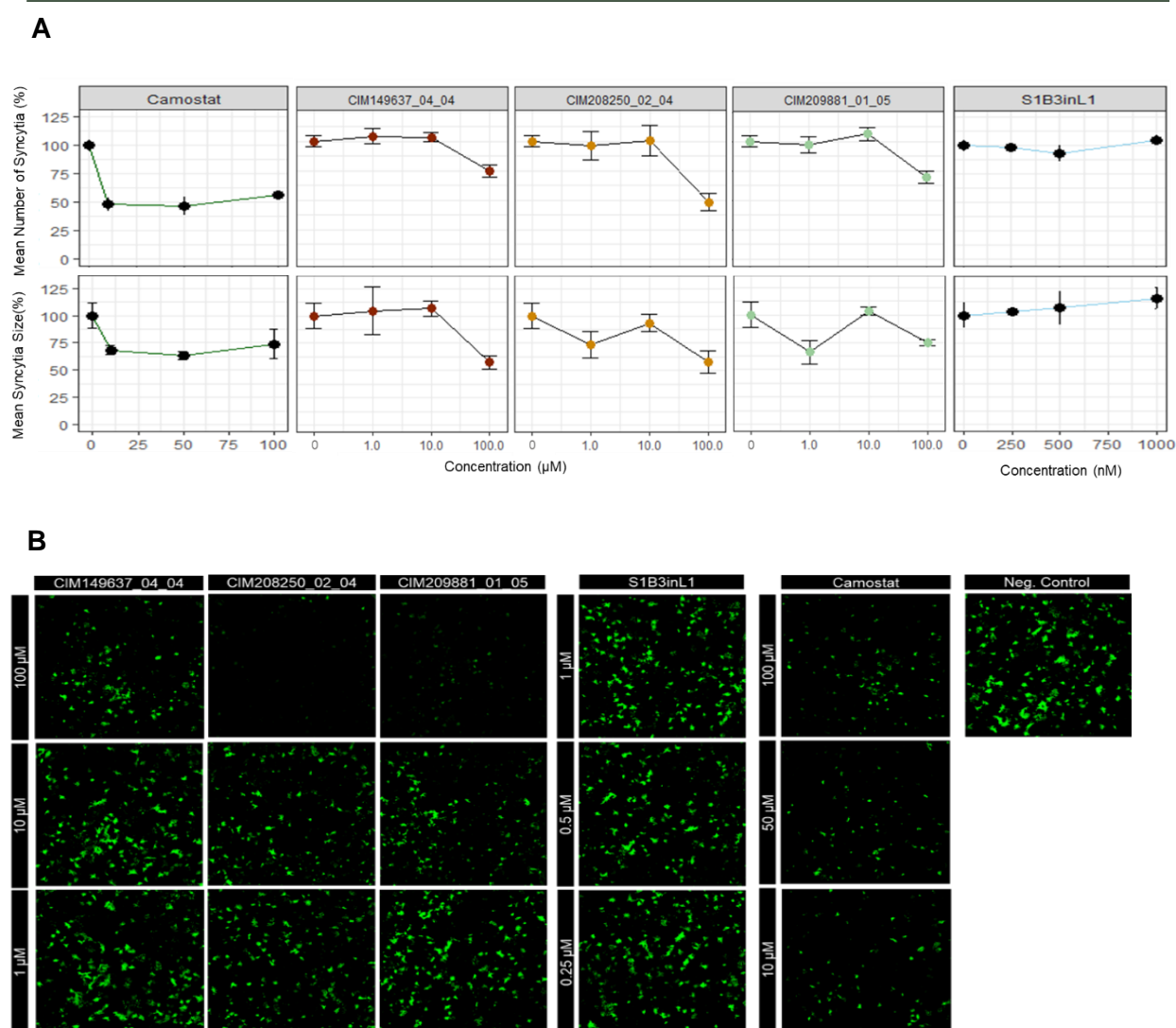
Figure 2.2. 4 – Testing of several CISTIM compounds and S1B3inL1 peptide in fusion assay. A) Graphical results of CISTIM compounds and S1B3inL1 peptide represented in mean syncytia size and mean number of syncytia per condition. Normalized for no treatment (100%). B) NIKON A1R images of the fusion assay. The most representative image is depicted. Fusion is visualized with GFP. Camostat is used as a positive control. Each condition is performed in triplicate. Imaging was done using NIKON A1R microscope and subsequently analysed with CellProfiler® software and RStudio.

UTRECHT UNIVERSITY, VIROLOGY DIVISION

(Fig. 2.2.4B, C). Similar inhibition as in the previous experiment was therefore not reached. As the fusion activity quickly stabilized after the addition of >6.25µM camostat, lower concentrations of the inhibitor were tested to further assess the critical inhibition region between 0-10 µM. A small reduction in syncytia number was noticeable after 0.1 µM, but the syncytia size decreased at >1 µM. Visually, fusion inhibition could be observed at >10 µM. Camostat has thus shown to be able to consistently inhibit fusion activity in this new assay format, albeit with fluctuating efficacy, and was therefore chosen as a reference compound for future experiments.

The cell-cell fusion assay can detect inhibition by several novel anti-SARS-CoV-2 compounds and peptides.

As the assay has shown an ability to detect inhibitory activity, the fusion inhibition potential of several antiviral compounds and peptides was assessed. The compounds developed by the Centre for Innovation and Stimulation of Drug Discovery (CISTIM) were recently shown to inhibit SARS-CoV-2[39]. The mode of action of these compounds is still to be determined and this cell-cell fusion assay may therefore provide more clarity on the mechanism behind SARS-CoV-2 inhibition. The compounds were added to the HEK293T cells in concentrations ranging from 0-100 µM in a similar manner as previously
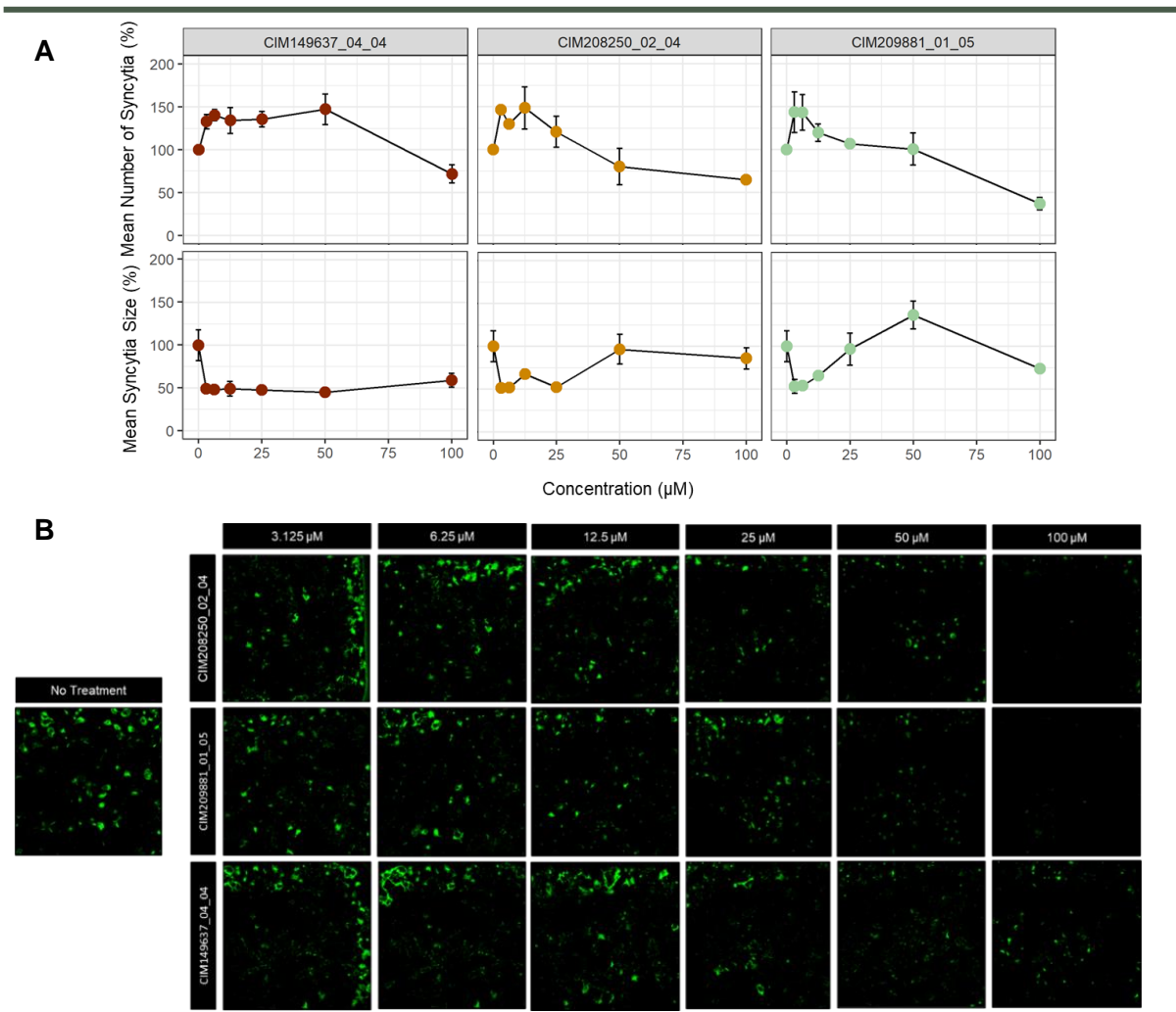
Figure 2.2. 5 – Concentration range of CISTIM compounds in fusion assay. Camostat was used as a positive control but did not show signs of fusion inhibition. Assay was performed in triplicate A) Graphical representation of fusion inhibition by CISTIM compounds. Normalized for no treatment (100%). The compounds inhibited the mean number of syncytia and CIM149637_04_04 showed signs of reduction in syncytia size. B) Fusion visualization. Most representative image is depicted. CISTIM compounds reduced fusion activity visibly after 25 µM. Samples are visualized by NIKON A1R and analysed with CellProfiler® software. Further data analysis is performed with RStudio.

described. Imaging and analysis were again performed with the NIKON A1R microscope and CellProfiler software. The compounds reached similar inhibition levels (20-50%) as camostat (Fig.2.2.5A, B) at 100 µM. As the fusion activity steeply declined between 10 and 100 µM, a range of concentrations between 10 and 100 µM was tested for the CISTIM compounds (Fig. 2.2.6). The CISTIM compounds did not show similar graphical results as during the first assay. The quantification was heavily influenced by the misidentification of syncytia by the CellProfiler algorithm. Syncytia were not fully formed, leading to large differences in intensity in a syncytium and a dotted-like structure. This results in the detection of several smaller syncytia instead of one larger syncytium (Fig. S2.5). Visually, inhibition by the CISTIM compounds could be observed. Imaging shows a reduction in fusion particularly after the addition of 25 µM of each compound.

Next, the fusion inhibition potential of a novel anti-spike macrocyclic peptide (S1B3inL1; manuscript in preparation) was assessed in the assay. As a control, a peptide (named HR2) preventing HR1-HR2 binding – therefore expected to reduce syncytia formation[40] – was included. Fusion inhibition could be well-observed after the addition of various concentrations of HR2 (0.03-3 µM). No syncytia were detected at 1 and 3 µM (Fig. 2.2.7A, B). S1B3inL1 was first tested at concentrations close to its IC_{50} of
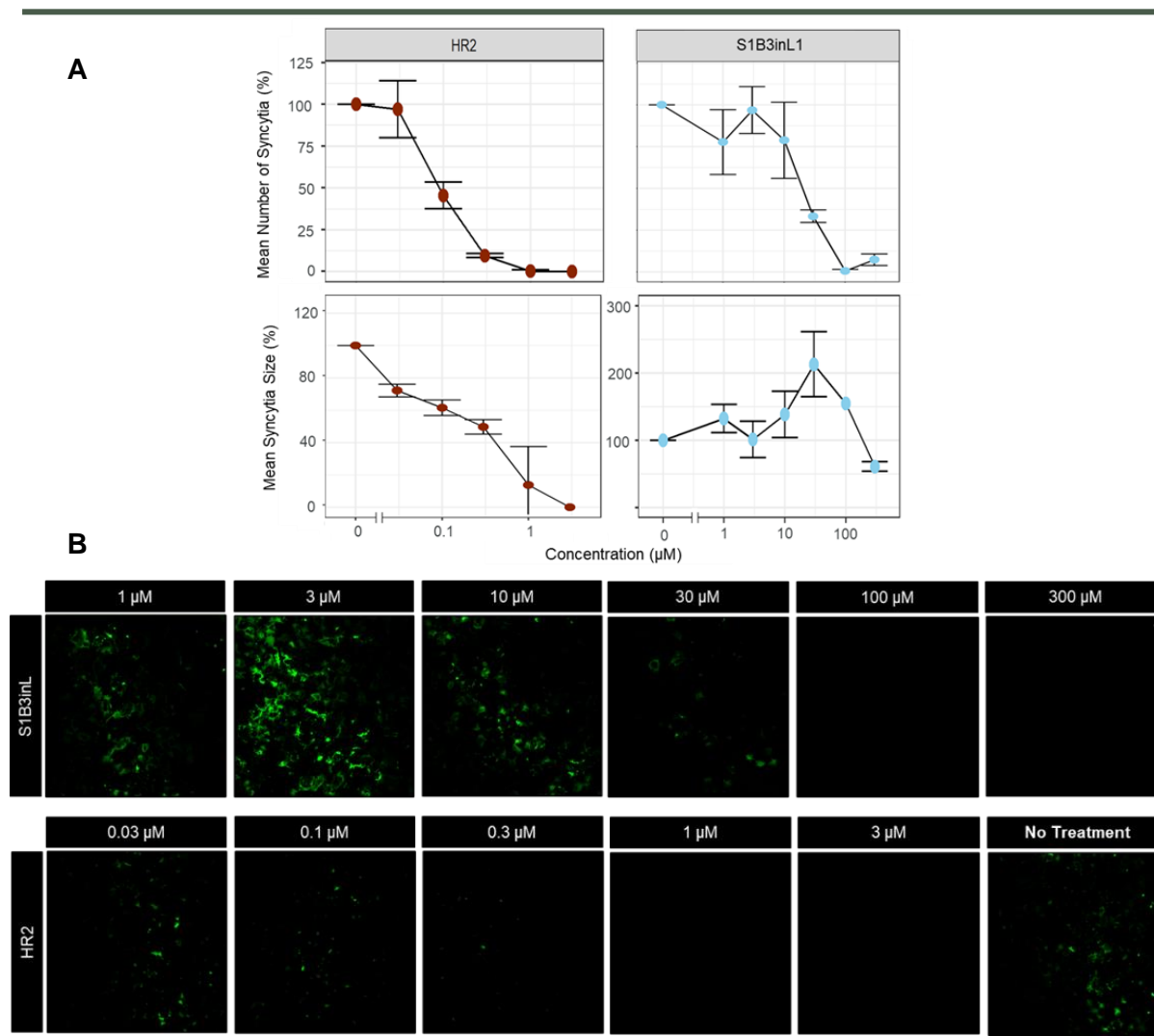
Figure 2.2. 6 – Fusion assay with S1B3inL1 concentration range. HR2 is included as positive controls. Conditions were performed in triplicate. A) Mean number of syncytia and mean syncytia size are given for various concentrations of S1B3inL1. Image analysis was performed using CellProfiler software and the data was processed in RStudio. B) Most representative picture is depicted. GFP+ syncytia were visualized with NIKON A1R microscopy (10x magnification). No fusion was detected for S1B3inL1 (100 and 300 µM) and HR2 (1 and 3 µM).

500 nM that was previously observed in virus neutralization assays, but it did not show any inhibition at the measured concentrations (Fig.2.2.5). With higher concentrations of the peptide (1-300 µM), a clear decrease in fusion activity could be observed (Fig. 2.2.7A, B). No fusion could be detected at the two highest concentrations (100 and 300 µM). Even though both peptides led to complete fusion inhibition, HR2 achieved this at considerably lower concentrations (1 µM (HR2) versus 100 µM (S1B3inL1)). This may be due to a difference in target area on the S-protein.

The CISTIM compounds and S1B3inL1 and HR2 peptides were all able to visibly prevent the formation of syncytia, indicating that the assay can detect and identify unestablished inhibitors of the SARS-CoV-2 entry pathway.

Discussion
The developed cell-cell fusion assay reaches high fusion levels, is easy to perform, and is capable of detecting inhibition by various compounds. VeroE6 cells with overexpression of TMPRSS2 showed considerably more fusion than wildtype VeroE6, highlighting the role of TMPRSS2 in fusion activity.

We assessed the usability of this assay in the identification of inhibitors targeting the SARS-CoV-2 entry pathway. First, Camostat has been shown to properly inhibit fusion in the assay and can act as a reference compound for this fusion assay (Fig.2.2.4). A similar fusion inhibition potency of camostat was previously shown[37]. After establishing a reference compound, various novel inhibitors were tested. The CISTIM compounds were able to successfully inhibit syncytia formation, indicating that these compounds act on the SARS-CoV-2 entry mechanism (Fig.2.2.5; Fig.2.2.6). The compounds generated visually more inhibition than camostat, but higher concentrations were needed. Lastly, an anti-spike peptide, S1B3inL1 had a previously observed IC_{50} of 500 nM in virus neutralization assays but showed fusion inhibition at >10 µM (Fig.2.2.7). The reference HR2 peptide showed greater potency, comparable to the IC_{50} (0.18 µM) that has been previously observed in a fusion assay[40]. This increased potency of HR2 compared to S1B3inL1 highlights the important role of HR1-HR2 binding in fusion activation. Both peptides were able to eliminate visual signs of fusion at higher concentrations.

The assay has been further optimized to improve assay performability by automating the data analysis and reducing the scale of the size to a 0.34 cm² well-format. However, imaging can still be time-consuming, and automated syncytia recognition can result in misidentification. This occurs particularly in cases of high fusion activity when individual syncytia are hard to distinguish from each other, and after the addition of inhibitory compounds as this may result in unidentifiable dotted-like GFP structures. The algorithm, therefore, has its limitations and is not able to provide accurate quantification of the syncytia.

Another limitation of the current quantification method is that it cannot account for the observed variations in cell distribution (as can be seen in Fig. 2.2.4C). Uneven distribution of cells will lead to changes in the morphology and the number of syncytia. For example, camostat was able to adequately inhibit syncytia formation repeatedly, but its quantified inhibition potency ranged from a 20 to 75% reduction in syncytia depending on experiments. As the current quantification method heavily depends on syncytia morphology, cell distribution could impact the outcome of the assay.

Alternatively, measuring fluorescent activity could provide a more rapid and accurate approach to fusion quantification. Most other fusion assays described in literature have resorted to measuring luminescence to quantify fusion activity [11,37,41–43]. Counting GFP+ pixels (with Amersham Typhoon Biomolecular Imager) is currently the only GFP complementation approach for SARS-CoV-2 described in literature[36] and reaches similar levels in fusion activity as the previously mentioned luciferase assays[11,37,41–43]. As we have further optimized the set-up of this assay, measuring fluorescent intensity

is expected to provide high levels of fusion comparable to or even greater than the currently developed fusion assays.

All in all, further optimization is needed for the fusion assay regarding quantification methodology. Measuring GFP intensity may provide a more accurate and rapid solution. Nevertheless, this assay can produce high levels of fusion, can be easily performed, and can properly identify SARS-CoV-2 inhibitors, making it a suitable assay for the detection of potential new inhibitors targeting the SARS-CoV-2 entry pathway.

3 CONCLUSION

We aimed to develop two cell-based assays for the evaluation of novel SARS-CoV-2 inhibitors, with each assay targeting a different component of the SARS-CoV-2 replication cycle. The cyclic luciferase M^{pro} assay did not reach high levels of activity after M^{pro} cleavage and is in its current state not suitable for inhibitor screening. However, this construct has been shown to function and several alterations to e.g. cell-type and cleavage site can be made that may improve the luciferase activity[29]. The cell-cell fusion assay was more successful as it was able to detect inhibition from several anti-virals. It was able to create high levels of fusion and identified camostat and HR2 as a suitable reference compound/peptide. However, quantification of this assay is limited as automated identification and area measurements of syncytia were shown to be inaccurate due to algorithmic limitations. Alterations in measurement methodology such as measuring GFP intensity may improve the accuracy of quantification.

Both assays can be safely operated in a BSL1/2 environment, are easy to perform, and are easily adaptable to suit other coronaviruses. Minor changes to the reporter construct are needed for the M^{pro} assay and the fusion assay can be easily adapted for suitable viruses (i.e. that can induce fusion and target the ACE2 receptor) by making alterations to suit the receptor-binding properties of the selected coronavirus[51,52].

Nevertheless, despite their limitations, these assays do show promise and may be applied for the successful identification and quantification of novel SARS-CoV-2 inhibitors after the necessary optimization steps have been completed.

UTRECHT UNIVERSITY, VIROLOGY DIVISION

4 METHODS

4.1 CELL-BASED M^PRO ASSAY

Cells and Plasmids

HEK293T and HeLa cells were cultured in DMEM + L-Glutamine and 4.5g/L Glucose (ref#: 12-741F; BioWhittaker®) with added 10% FBS (ref#: DE14-801FI; BioWhittaker) at 37°C + 5% CO_2. Cell passaging was performed using 0.05% Trypsin-EDTA (ref# TRY-4B; Capricorn Scientific) and Dulbecco's PBS (ref# PBS-1A; Capricorn Scientific).

WT M^pro is encoded in pBIND-Mpro-VP16 (SARS2) (constructed in this lab) containing a CMV promotor, GAL4BD, VP16AD, and RLuc. Mutant M^pro (C145A) was added in a similar plasmid: pBIND-Mpro[C145A]-VP16 (SARS2) (constructed in this lab). pcDNA_RFP-TEVprotease (ref#: 124947; Addgene) and pcDNA3_Cycluc_TEVS (ref#: 119207; Addgene) were obtained from Addgene. M^pro CycLuc was created by replacing the TEV cleavage site in TEV CycLuc with the M^pro cleavage site: *AAGGCCAAGAAGGGATCCGTTGCTAGATTGCA   GAGTGGTTTCGGCGGTGCCAAAAACATT*. The OSBP plasmid (pCMV-OSBP[S381A]) containing the HIS-tag was present in this lab.

Luciferase Assay

After treatment with 50 μL/well 5% Poly-L-Lysin (ref#: SLCJ5847; Sigma Aldrich), HEK293T cells were plated in a flat-bottom 96-well plate (ref#: 3599; Corning Incorporated) at a density of 15000 cells/well in 100 μL of assay medium and incubated for 24h at 37°C + 5% CO_2. Transfection mixes were made with Lipofectamine®2000 (ref#: 11668-019; Invitrogen), Opti-MEM® 1x + GlutaMAX^TM (ref#: 51985-026; gibco), and 50 ng CycLuc and 50 ng protease (unless stated otherwise). The cells were transfected with 10 μL/well of the designated transfection mix with each condition performed in triplicate. After transfection, the cells were incubated for 24h, 48h, or 72h (as previously stated) at 37°C + 5%. TEVp expression (mCherrry) was measured with EVOS fl (AMG) 24h and 48h post-transfection. After the designated incubation time, the cells were lysed with 5x Passive Lysis Buffer (25 μL/well) (ref#: E194A; Promega) for 30 minutes at room temperature (RT). After lysis, 10 μL of each well was transferred to a white 96-well plate (Greiner Bio-One). FLuc and RLuc activity were visualized with GloMax® Explorer (ref#: GM3510; Promega) using the Dual-Luciferase® Reporter Assay System (ref#: E1980; Promega) with LARII (FLuc) and Stop&Glo (RLuc) buffers (both 40 μL/well). Data were plotted with GraphPad Prism V9.3.1 and normalized for RLuc activity. RLuc activity could not be measured for the assay with TEVp. For these assays, 60 μL 5x passive lysis buffer was added to each well with an incubation of 30 min/RT. 25 μL lysate was transferred to a white 96-well plate. Luciferase activity was measured with a buffer containing 50% UU-FLAR basic buffer (10% 1M Tricine (pH8); 2% 10mM EDTA; 10% 50 mM $MgSO_4$; 78% MilliQ), 3.5% MilliQ, 1% 1M DTT, 1.25% 100 mM ATP, and 12.5% 100 μM D-luciferin (100 μL/well).

Western Blotting

HEK cells were plated in a 6-well plate at a density of 1.2×10^6 cells/well with one well per condition and cultured overnight at 37°C + 5% CO_2. For transfection, 1000 ng DNA (or 2500 ng when indicated) was added per well together with 10 μL Lipofectamine®2000 (ref#: 11668-019; Invitrogen). Samples were cultured for 24h, 48h, or 72h (as previously stated) after which the medium was removed, and the cells were collected in 1.5 mL PBS (ref# PBS-1A; Capricorn Scientific). Cells were centrifuged and lysed with RIPA lysis buffer + cOmplete Mini (ref#: 11836153001; Roche Diagnostics). Cell debris was removed, and protein concentration was measured with Micro BCA^TM Protein Assay Kit (ref#: 23235; ThermoFisher). SDS PAGE samples consisted of 5x Laemmli buffer, 100 ng protein, and RIPA buffer. Samples were heat-denatured for 7-10 minutes at 95°C and cooled to room temperature.

23

Subsequently, the samples were added to a 12.5% 1.5mm gel (Running gel: 1.25 mL Lower Buffer; 2.5 mL AB40% (ref#: 1610148; Bio-Rad); 5.5 mL MilliQ; 0.1 mL 10% SDS; 0.5 mL 1% TEMED (ref#: 35925.01; Serva); 0.15 mL 10% APS. Stacking gel: 1.25 mL Upper Buffer; 0.5 mL AB40% (ref#: 1610148, Bio-Ra d); 2.95 mL MilliQ; 0.05 mL 10% SDS; 0.25 mL 1% TEMED (ref#: 35925.01; Serva); 0.15 mL 10% APS) and run at 100V. The gel was then transferred to a nitrocellulose membrane (ref#: 1704158; Bio-Rad) and blotted for 10 minutes with the 1.5mm gel protocol on the Trans-Blot® Turbo™ (Bio-Rad) Thereafter, the membrane was blocked in 5% skim milk (Nutricia Protifar) in PBS-T (5x phosphate buffer saline tablet (ref#: P4417; Sigma-Aldrich), 1 L MilliQ, 1% Tween® 20 (ref#: 8.22184; Sigma-Aldrich)), after which it was stained with 6x-HIS Tag Antibody (1:500) (ref#: MA1-21315; ThermoFisher) or 6x-HIS Tag Monoclonal Antibody, HRP (1:500) (ref#: MA1-21315-HRP; ThermoFisher) in 1% skim milk/PBS-T overnight at 4°C and 45 rpm. Secondary staining was performed with IRDye® 680RD Goat anti-Mouse IgG (1:10 000) (ref#: 926-68070; LiCor) at room temperature for 2h. The blot was visualized with Odyssey Fc (LiCor). Before visualization, the membrane stained with anti-HIS-HRP was treated with Pierce™ ECL Western Blotting Substrate (ref#: 32209; ThermoFisher). The membrane was stripped with 0.2M NaOH and reblotted with beta-actin (1:30 000) for 2h at room temperature, after which it was stained with a Goat anti-Mouse secondary antibody and visualized with Odyssey Fc. The membrane was washed 3x10 minutes with PBS-T in between staining.

Immunofluorescence Assay
12 mm Cover Slips (ref#: CB00120RA120MNZ0; epredia) were added to a 24-well plate and washed with 100% EtOH. 300 µL 5% Poly-L-Lysin (ref#: SLCJ5847; Sigma Aldrich) was added to each well before plating HeLa cells at a density of 90 000 cells/well. After 24h, the cells were transfected with 300 ng DNA using 3 µL/well Lipofectamine®2000 (ref#: 11668-019; Invitrogen). 24h, 48h, or 72h post-transfection, the cells were fixed with 200 µL 4% PFA (ref#: 104003; Merck) and permeabilized with PBS/0.1% Triton® X100 (ref#: 93426; Fluka). 6x-HIS Tag Antibody (ref#: MA1-21315; ThermoFisher) was diluted 1:500 in PBS + 2% NGS. A droplet of the antibody dilution was pipetted on the coverslip followed by a 45-minute incubation period at room temperature. Thereafter, the coverslips were washed with PBS twice. The secondary antibody (488 Goat Anti Mouse (ref#: A11001; Invitrogen)), was diluted 1:400 in PBS + 2% NGS + 1:1000 DAPI and added to the coverslips. After 45 minutes at room temperature, the coverslips were washed twice with PBS and mounted on µscope slides (ref#: 16245172; epredia) with Fluorsave™ Reagent (ref#: 345789-20ML; Merck). The results were visualized with either EVOS fl (AMG) or an Olympus BX60 WF microscope.

4.2   CELL-CELL FUSION ASSAY

Cells, plasmids, and antibodies
VeroE6 and VeroE6 TMPRSS2+ (+GFPS(1-10) cell lines were obtained from the Haagmans Group, Erasmus UMC and cultured in DMEM + GlutaMAX™ (ref#: 31966-021; gibco) with 10% FBS (ref#: DE14-801FI; BioWhittaker), 1% Penicillin/Streptomycin, 250 µg/mL G418, 125 µg/mL Hygro (TMPRSS2+ cells only) at 37°C + 5% CO2. Cell passaging was performed using 0.2% Trypsin-EDTA (ref#:15400-054; gibco) diluted in Dulbecco's PBS (ref# PBS-1A; Capricorn Scientific).

HEK293T cells were cultured in DMEM + L-Glutamine and 4.5g/L Glucose (ref#: 12-741F; BioWhittaker®) with added 10% FBS (ref#: DE14-801FI; BioWhittaker) at 37°C + 5% CO2. Cell passaging was performed using 0.05% Trypsin-EDTA (ref# TRY-4B; Capricorn Scientific) and Dulbecco's PBS (ref# PBS-1A; Capricorn Scientific).

pGAGGS_Bactin_INSGSG_7xGFP11_P2A_linker_3xNLS_TagBFP_EcoR1_BglII; pCAGGS 2019-nCoV-S Copt, pCAGGS_Empty were obtained from the Haagmans Group, Erasmus UMC.

Biotinylated Human ACE2, Fc, Avitag™ was obtained from Acro Biosystems (ref#: AC2-H82F9). REGN#10933 was retrieved from *Hansen et al., 2020,* and camostat was bought from MedChemExpress (ref#: HY-13512) The CISTIM compounds (CIM149637_04_04, CIM208250_02_04, CIM209881_01_05) were developed by this lab in collaboration with the Centre for Innovation and Stimulation of Drug Discovery (CISTIM). The S1B3inL1 peptide was developed in this lab and synthesized by the Jongkees Research Group, VU. The HR2 peptide was obtained from *Xia et al., 2020*[40].

Fusion Assay
HEK293T cells were plated at a density of 1.5×10^6 cells/well in a 6-well plate and incubated overnight at 37°C + 5% CO2. After 24h, the cells were transfected with 3 µg of pGAGGS_Bactin_GFP11, and either pGAGGS-spike or pGAGGS-empty using PEI in a ratio of 1:3 (plasmid: PEI). Simultaneously, VeroE6 cells were plated at a density of either 36 000 cells/well (18-well Glass Bottom Microslide (ref#: 81817; IBIDI)) or 800 000 to 200 000 cells/well (24-well plate (ref#: 3524; Corning Incorporated)). For the 24-well plate, 12 mm Cover Slips (ref#: CB00120RA120MNZ0; epredia) were first placed in each well and washed with 100% EtOH. Both plates were incubated overnight at 37°C + 5% CO2. Following the incubation period, several methods were applied.

For the coverslips-based assay, the medium from the VeroE6 cells was removed and 0.2% Trypsin-EDTA (ref#:15400-054; gibco) was added to 1 well designated for counting. VeroE6 cells from that well were collected and counted. The medium from the HEK293T cells was removed and the cells were collected in 1mL Opti-MEM® 1x + GlutaMAX™ (ref#: 51985-026; gibco) and counted. The inhibitor (if needed) was added to 300 microL Opti-MEM® and further diluted via serial dilution. The designated number of HEK293T cells was added to the samples. The solution was added to the plated VeroE6 cells and incubated at room temperature for 20 minutes, and subsequently incubated overnight at 37°C + 5% CO2. Cells were fixed with 200 microL 4% PFA (ref#: 104003; Merck) and mounted on microscope slides (ref#: 16245172; epredia) with Fluorsave™ Reagent (ref#: 345789-20ML; Merck). Fusion activity was visualized by imaging 6-12 frames (BFP and GFP) (20x magnification) with an Olympus BX60 WF microscope. Nuclei were counted per image and data was visualized with GraphPad Prism V9.3.1.

A similar procedure was followed for the IBIDI microslides with several deviations. VeroE6 cells were not counted after plating and after fixation, the cells were kept on the slide in PBS. The assay was performed in triplicate. Visualization was performed with NIKON A1R/STORM by creating a large image (4x4 frames) of each well with the GFP channel at 10x magnification. Images were analyzed by CellProfiler™ software for syncytia detection. Syncytia were identified based on GFP signaling and size (between 15- and 50 000-pixel units). Area measurements were performed in pixel units. Syncytia touching the image border were not included in the analysis. The data were further processed in RStudio. For each image, the total number and median size were calculated. For each condition, the mean number and mean size were calculated from the outcomes of each replicate. The empty vector was not included in these experiments.

REFERENCES

1.   WHO Coronavirus (COVID-19) Dashboard | WHO Coronavirus (COVID-19) Dashboard With Vaccination Data. https://covid19.who.int/.

2.   Hu, B., Guo, H., Zhou, P. & Shi, Z. L. Characteristics of SARS-CoV-2 and COVID-19. *Nat. Rev. Microbiol.* **19**, 1 (2021).

3.   Wang, D. *et al.* Clinical Characteristics of 138 Hospitalized Patients With 2019 NovelCoronavirus–Infected Pneumonia in Wuhan, China. *JAMA* **323**, 1061 (2020).

4.   WHO Director-General's opening remarks at the media briefing on COVID-19 - 11 March 2020. https://www.who.int/director-general/speeches/detail/who-director-general-s-opening-remarks-at-the-media-briefing-on-covid-19---11-march-2020.

5.   Ecdc. Partial COVID-19 vaccination, vaccination following SARS-CoV-2 infection and heterologous vaccination schedule: summary of evidence Key messages Partial vaccination. (2021).

6.   Chitsike, L. & Duerksen-Hughes, P. Keep out! SARS-CoV-2 entry inhibitors: their role and utility as COVID-19 therapeutics. *Virol. J.* **18**, 1–17 (2021).

7.   Tao, K. *et al.* SARS-CoV-2 Antiviral Therapy. *Clin. Microbiol. Rev.* **34**, (2021).

8.   European Medicines Agency. COVID-19 treatments . https://www.ema.europa.eu/en/human-regulatory/overview/public-health-threats/coronavirus-disease-covid-19/treatments-vaccines/covid-19-treatments.

9.   An, W. F. & Tolliday, N. Cell-Based Assays for High-Throughput Screening. *Mol. Biotechnol. 2010 452* **45**, 180–186 (2010).

10.   Michelini, E., Cevenini, L., Mezzanotte, L., Coppa, A. & Roda, A. Cell-based assays: fuelling drug discovery. *Anal. Bioanal. Chem. 2010 3981* **398**, 227–238 (2010).

11.   Zhao, M. *et al.* Rapid, reliable, and reproducible cell fusion assay to quantify SARS-Cov-2 spike interaction with hACE2. *PLOS Pathog.* **17**, e1009683 (2021).

12.   Kilianski, A. & Baker, S. C. Cell-based antiviral screening against coronaviruses: Developing virus-specific and broad-spectrum inhibitors. *Antiviral Res.* **101**, 105–112 (2014).

13.   Malone, B., Urakova, N., Snijder, E. J. & Campbell, E. A. Structures and functions of coronavirus replication–transcription complexes and their relevance for SARS-CoV-2 drug design. *Nat. Rev. Mol. Cell Biol. 2021 231* **23**, 21–39 (2021).

14.   Murgolo, N. *et al.* SARS-CoV-2 tropism, entry, replication, and propagation: Considerations for drug discovery and development. *PLoS Pathogens* vol. 17 e1009225 (2021).

15.   Cai, Y. *et al.* Distinct conformational states of SARS-CoV-2 spike protein. *Science (80-.).* **369**, (2020).

16.   Das, G. *et al.* An overview of key potential therapeutic strategies for combat in the COVID-19 battle. *RSC Adv.* **10**, 28243–28266 (2020).

17.   Emrani, J. *et al.* SARS-COV-2, infection, transmission, transcription, translation, proteins, and treatment: A review. *Int. J. Biol. Macromol.* **193**, 1249–1273 (2021).

18.   Ning, S., Yu, B., Wang, Y. & Wang, F. SARS-CoV-2: Origin, Evolution, and Targeting Inhibition. *Front. Cell. Infect. Microbiol.* **11**, 530 (2021).

19.   Amin, S. A., Banerjee, S., Ghosh, K., Gayen, S. & Jha, T. Protease targeted COVID-19 drug discovery and its challenges: Insight into viral main protease (Mpro) and papain-like protease (PLpro) inhibitors.

REFERENCES

Bioorganic Med. Chem. **29**, 115860 (2021).

20. Zhang, L. *et al.* Crystal structure of SARS-CoV-2 main protease provides a basis for design of improved α-ketoamide inhibitors. *Science (80-.).* **368**, (2020).

21. Ambike, S. *et al.* Targeting genomic SARS-CoV-2 RNA with siRNAs allows efficient inhibition of viral replication and spread. *Nucleic Acids Res.* (2021) doi:10.1093/NAR/GKAB1248.

22. Eymieux, S. *et al.* Secretory vesicles are the principal means of sars-cov-2 egress. *Cells* **10**, 2047 (2021).

23. Ghosh, R., Chakraborty, A., Biswas, A. & Chowdhuri, S. Potential therapeutic use of corticosteroids as SARS CoV-2 main protease inhibitors: a computational study. *J. Biomol. Struct. Dyn.* 1 (2020) doi:10.1080/07391102.2020.1835728.

24. Sacco, M. D. *et al.* Structure and inhibition of the SARS-CoV-2 main protease reveal strategy for developing dual inhibitors against Mpro and cathepsin L. *Sci. Adv.* **6**, (2020).

25. Steuten, K. *et al.* Challenges for Targeting SARS-CoV-2 Proteases as a Therapeutic Strategy for COVID-19. *ACS Infect. Dis.* (2021) doi:10.1021/acsinfecdis.0c00815.

26. Mengist, H. M., Dilnessa, T. & Jin, T. Structural Basis of Potential Inhibitors Targeting SARS-CoV-2 Main Protease. *Front. Chem.* **9**, 7 (2021).

27. Van Der Linden, L. *et al.* Application of a cell-based protease assay for testing inhibitors of picornavirus 3C proteases. *Antiviral Res.* **103**, 17–24 (2014).

28. T, F. *et al.* Design of fast proteolysis-based signaling and logic circuits in mammalian cells. *Nat. Chem. Biol.* **15**, 115–122 (2019).

29. Moghadasi, S. A. *et al.* Gain-of-function assay for SARS-CoV-2 Mpro inhibition in living cells. *bioRxiv* (2020) doi:10.1101/2020.11.09.375139.

30. Chen, K. *et al.* A highly sensitive cell-based luciferase assay for high-throughput automated screening of SARS-CoV-2 nsp5/3CLpro inhibitors. *bioRxiv* 2021.12.18.473303 (2021) doi:10.1101/2021.12.18.473303.

31. Rawson, J. M. O., Duchon, A., Nikolaitchik, O. A., Pathak, V. K. & Hu, W.-S. Development of a Cell-Based Luciferase Complementation Assay for Identification of SARS-CoV-2 3CLpro Inhibitors. *Viruses* **13**, (2021).

32. Kanno, A., Yamanaka, Y., Hirano, H., Umezawa, Y. & Ozawa, T. Cyclic Luciferase for Real-Time Sensing of Caspase-3 Activities in Living Mammals. *Angew. Chemie Int. Ed.* **46**, 7595–7599 (2007).

33. Mathieu, C. *et al.* A bioluminescent 3clpro activity assay to monitor sars-cov-2 replication and identify inhibitors. *Viruses* **13**, 1814 (2021).

34. Chuck, C. P. *et al.* Profiling of Substrate Specificity of SARS-CoV 3CLpro. *PLoS One* **5**, (2010).

35. Zhao, Y. *et al.* Structural basis for replicase polyprotein cleavage and substrate specificity of main protease from SARS-CoV-2. *Proc. Natl. Acad. Sci.* **119**, (2022).

36. Mykytyn, A. Z. *et al.* SARS-CoV-2 entry into human airway organoids is serine protease-mediated and facilitated by the multibasic cleavage site. *Elife* **10**, 1–23 (2021).

37. BF, H. *et al.* SARS-CoV-2 and SARS-CoV Spike-Mediated Cell-Cell Fusion Differ in Their Requirements for Receptor Expression and Proteolytic Activation. *J. Virol.* **95**, (2021).

38. Hansen, J. *et al.* Studies in humanized mice and convalescent humans yield a SARS-CoV-2 antibody cocktail. *Science (80-.).* **369**, 1010–1014 (2020).

REFERENCES

39.   Bardiot, D. *et al.* Synthesis, Structure–Activity Relationships, and Antiviral Profiling of 1-Heteroaryl-2-Alkoxyphenyl Analogs as Inhibitors of SARS-CoV-2 Replication. *Molecules* **27**, 1052 (2022).

40.   Xia, S. *et al.* Fusion mechanism of 2019-nCoV and fusion inhibitors targeting HR1 domain in spike protein. *Cell. Mol. Immunol.* **17**, 765 (2020).

41.   Theuerkauf, S. A. *et al.* Quantitative assays reveal cell fusion at minimal levels of SARS-CoV-2 spike protein and fusion from without. *iScience* **24**, 102170 (2021).

42.   Yu, S. *et al.* SARS-CoV-2 spike engagement of ACE2 primes S2' site cleavage and fusion initiation. *Proc. Natl. Acad. Sci. U. S. A.* **119**, e2111199119 (2022).

43.   Zhu, Y., Yu, D., Yan, H., Chong, H. & He, Y. Design of Potent Membrane Fusion Inhibitors against SARS-CoV-2, an Emerging Coronavirus with High Fusogenic Activity. *J. Virol.* **94**, (2020).

44.   MacDonald, E. A. *et al.* Recognition of Divergent Viral Substrates by the SARS-CoV-2 Main Protease. *ACS Infect. Dis.* **7**, 2591–2595 (2021).

45.   Li, F. Receptor Recognition Mechanisms of Coronaviruses: a Decade of Structural Studies. *J. Virol.* **89**, 1954 (2015).

46.   Leroy, H. *et al.* Virus-Mediated Cell-Cell Fusion. *Int. J. Mol. Sci. 2020, Vol. 21, Page 9644* **21**, 9644 (2020).
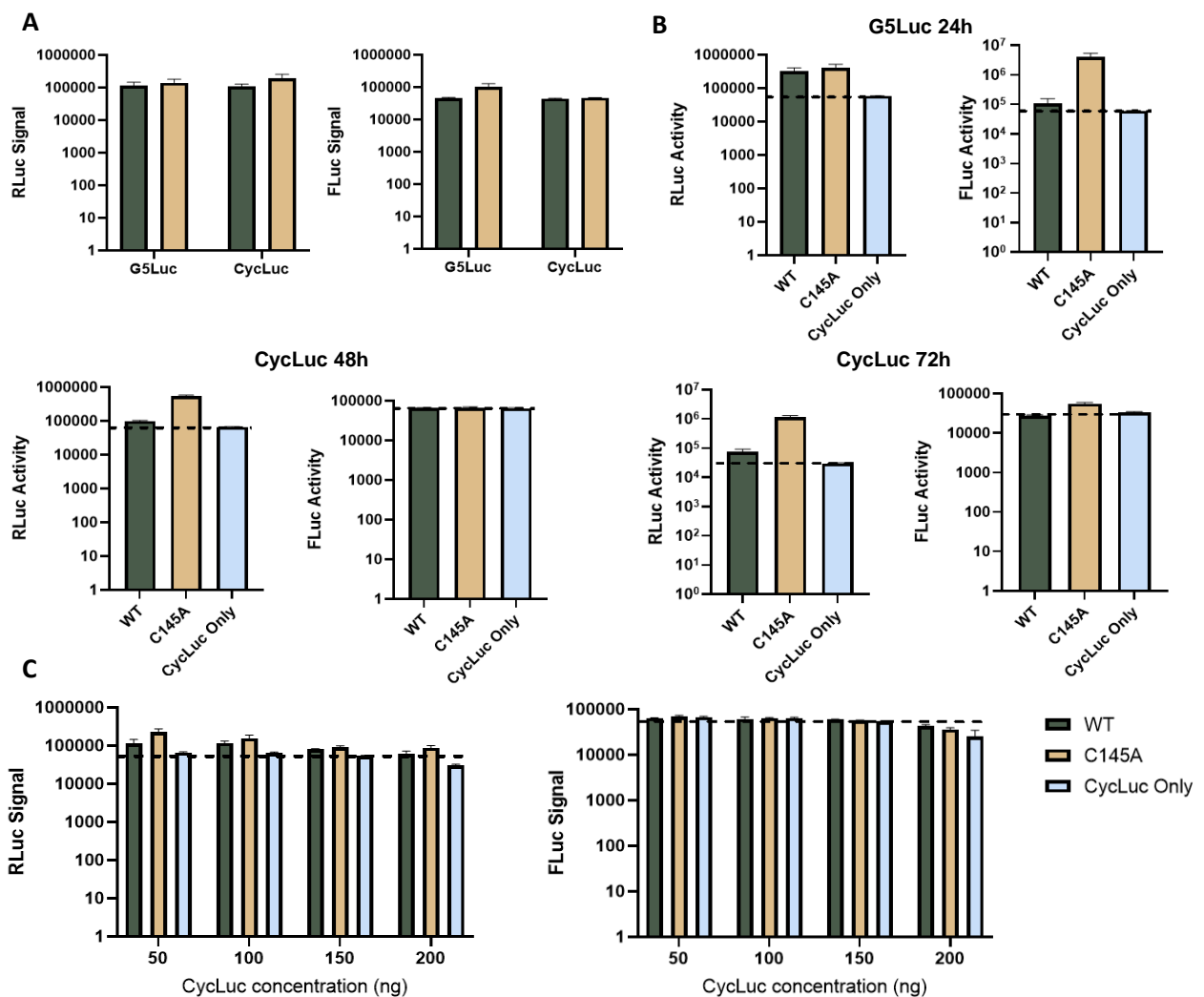
CELL-BASED M^PRO ASSAY

Plasmid Maps

| Plasmid	Map
WT Mpro VP16	pBIND-Mpro-VP16 (SARS2)
Mpro CycLuc	Mpro CycLuc-HIS
TEV CycLuc	TEV CycLuc-HIS
TEV protease mCherry	TEVp-mCherry
G5Luc	pG5luc.gb.dna

Plasmid maps can be found in the VIRshare

Supplementary Luciferase Data

S1.1

Figure S1. 1 – Raw data of Renilla (RLuc) and Firefly (FLuc) luciferases. Background signals are illustrated with dotted lines. HEK293T cells were co-transfected with cyclic luciferase and wild-type (WT), C145A (inactive) mutant, or no M^pro (CycLuc only). *Firefly* (FLuc) and *Renilla* (RLuc) luciferase activity were visualized with the GloMax® Explorer using the Dual-Luciferase® Reporter Assay System. A) G5Luc versus CycLuc comparison assay with WT and C145A M^pro. B) Raw data from the assay using various transfection times for CycLuc. G5Luc (24h transfection time) is included as control. C) Variations in CycLuc concentrations with either WT, C145A, or no M^pro.

S1.2
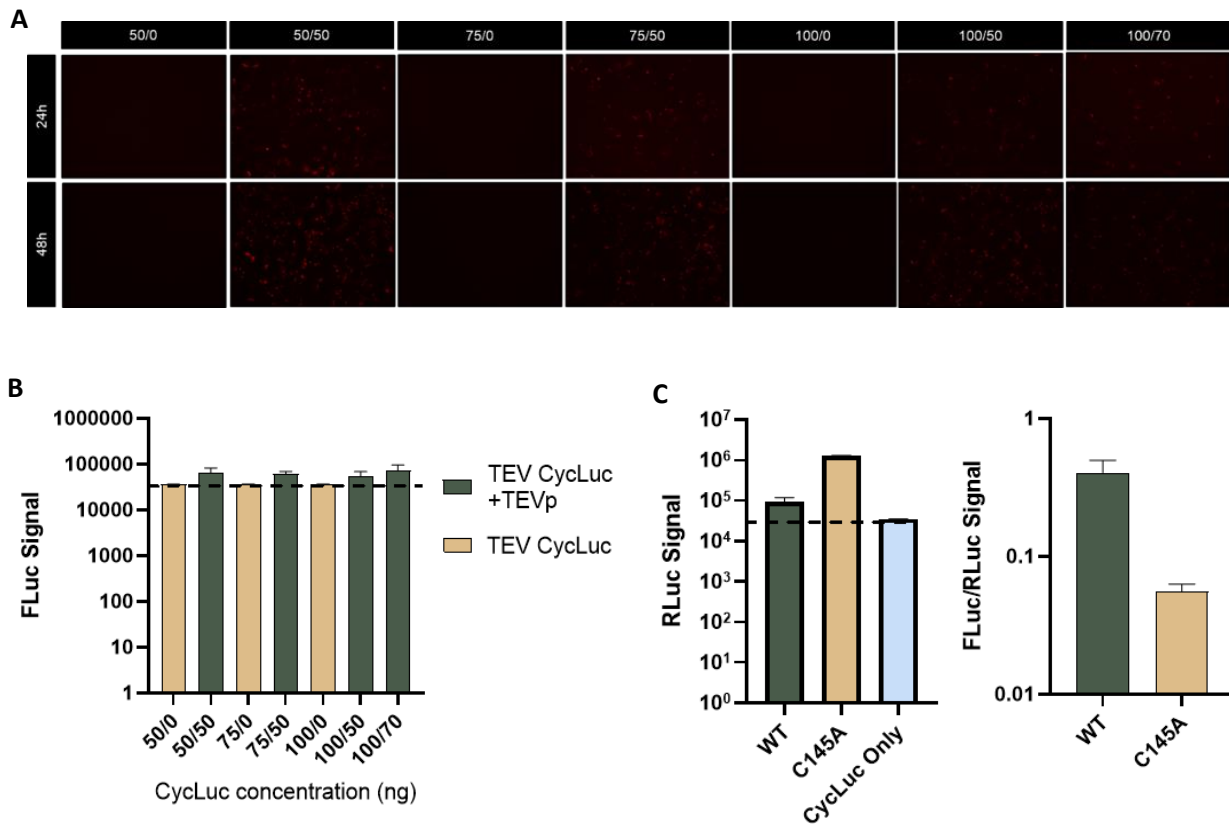
Figure S1. 2 – TEV CycLuc activity in comparison with M^{pro} CycLuc. HEK293T cells were co-transfected with cyclic luciferase and wildtype (WT) or C145A (inactive) mutant, or no M^{pro} (CycLuc Only). *Firefly* (FLuc) and *Renilla* (RLuc) luciferase activity were visualized with the GloMax® Explorer using the Dual-Luciferase® Reporter Assay System. A) Visualization of transfection efficiency of TEV protease with mCherry for various TEV CycLuc/TEV protease concentration ratios after 24 and 48 hours. Measured with the Evos fl microscope. B) FLuc signal for TEV CycLuc for various TEV CycLuc/TEV protease (TEVp) concentration ratios. Background activity is illustrated with a dotted line. C) RLuc signal (left) for the M^{pro} plasmids (WT); C145A and no M^{pro} (CycLuc Only)). Background noise is indicated with a dotted line. Right: FLuc/RLuc signal) of the WT and C145A M^{pro} after addition of M^{pro} CycLuc.

Raw Data

| Experiment	Data Type	Raw Data
G5Luc vs M^{pro} CycLuc	GloMax® Output	G5Luc vs Mpro CycLuc (folder)
M^{pro} CycLuc concentration variations	GloMax® Output	Mpro CycLuc concentration variations (folder)
Transfection time variations	GloMax® Output	Transfection time variations (folder)
TEV CycLuc/TEV protease concentrations	GloMax® Output	TEVp concentration variations (folder)
TEV CycLuc vs M^{pro} CycLuc	GloMax® Output	Mpro CycLuc vs TEV CycLuc (folder)

CELL-CELL FUSION ASSAY

Plasmid Maps

| Plasmid	Map
Bactin_BFP_GFP11	Bactin_GSG_7xGFP11_INS_GSG_P2A_linker_3xNLS_TagBFP_EcoRI_BglII_pCAGGS.dna
pCAGGS 2019-nCoV-S Copt	Genscript_Copt_S_SARS-CoV-2.dna
pCAGGS_Empty	pcaggsFrei.gb

Supplementary Fusion Data

S2.1
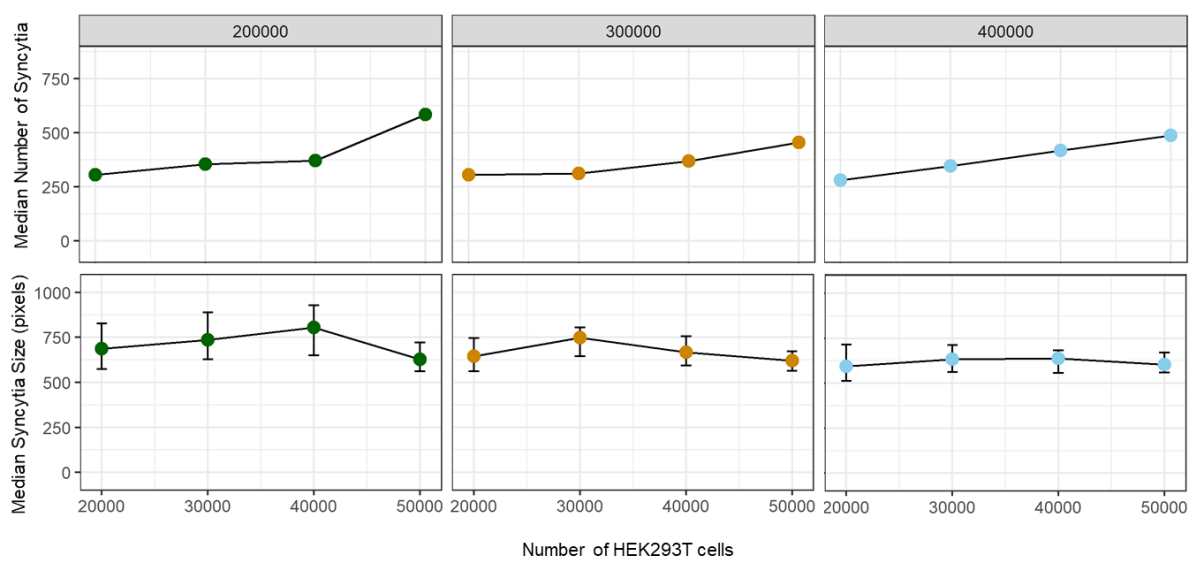
Figure S2. 1 – Determination of HEK293T/VeroE6 cell ratio on coverslips. Fusion activity was measured for several combinations of HEK293T (20,000/30,000/40,000/50,000) and VeroE6 cells (200,000/300,000/400,000). The VeroE6 cells were plated on 12 mm coverslips and incubated for a day before the HEK293T (+S-protein) cells were added. To allow for sufficient fusion activity, the cells were left overnight at 37°C. Imaging was performed the next day after fixation of the cells with the NIKON A1R/STORM microscope and analysed with CellProfiler software. Data was processed in RStudio.

UTRECHT UNIVERSITY, VIROLOGY DIVISION

S2.2
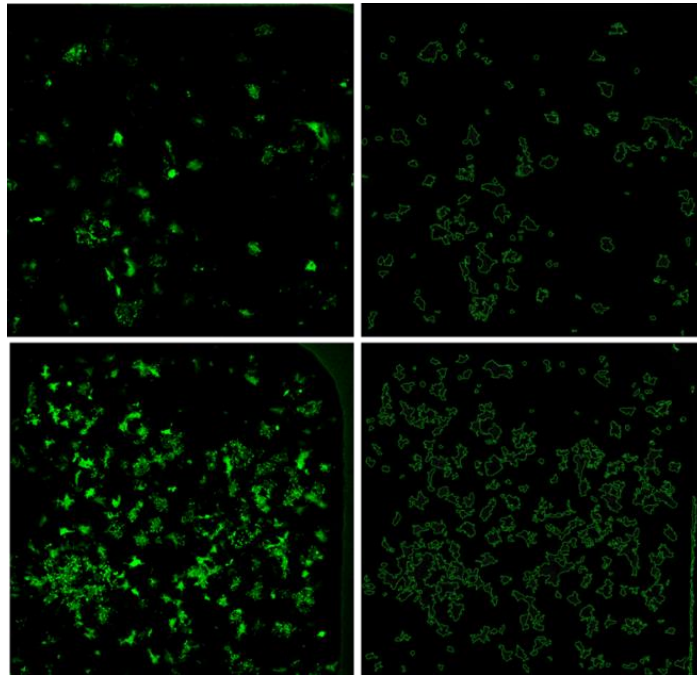
Figure S2. 2 – CellProfiler can recognise the syncytia based on shape and fluorescent intensity. Syncytia touching the border of the image are not included in the analysis. Clearly separated syncytia are easily identified (top), whilst with crowded syncytia the algorithm has more difficulty (bottom). The walls of the well are not or barely included in the analysis.

S2.3
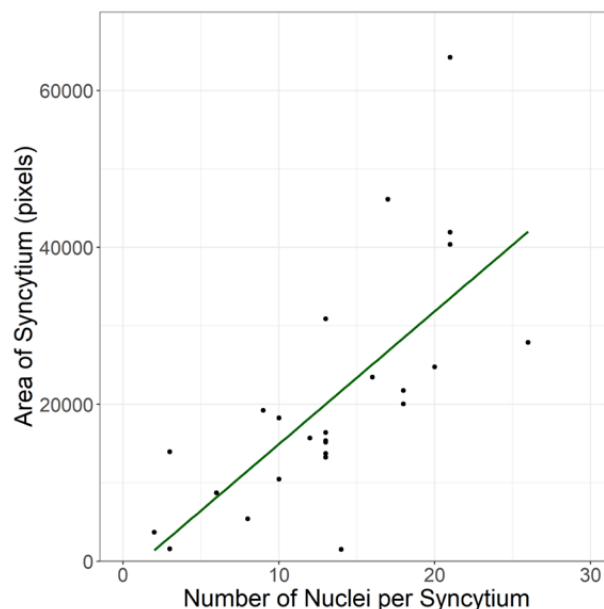
Figure S2. 1 – Relationship between the area and number of nuclei of a syncytium. The nuclei of several syncytia of varying sizes have been counted manually. The size of each syncytium is analysed by CellProfiler (area in pixels). A correlation between the two factors can be observed. The VeroE6 cells were plated on 12 mm coverslips and incubated for a day before the HEK293T (+S-protein) cells were added (ratio: 20 000/200 000 (HEK293T:VeoE6)). To allow for sufficient fusion activity, the cells were left overnight at 37°C. Imaging was performed with NIKON A1R microscopy (20x magnification) after fixation of the cells and analysed with CellProfiler software. Data was processed in RStudio.

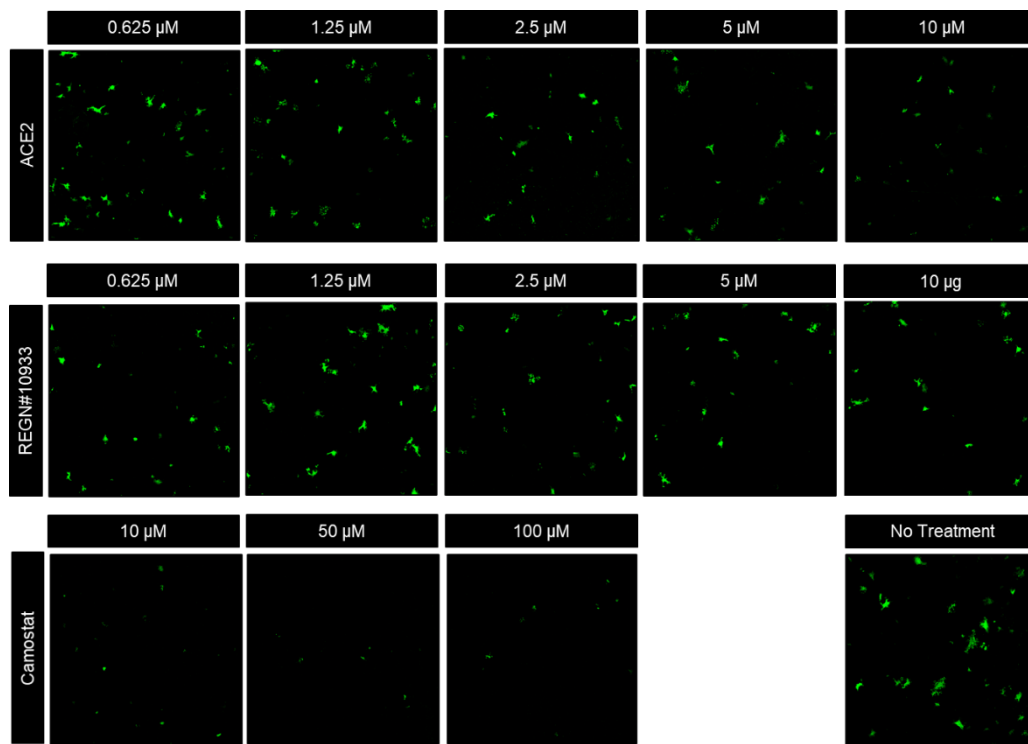UTRECHT UNIVERSITY, VIROLOGY DIVISION

S2.4

Figure S2. 3 – Visualization of fusion assay with hACE2, REGN#10933, and camostat. The VeroE6 cells were plated on 12 mm coverslips and incubated for a day before the HEK293T (+S-protein) cells were added (Ratio: 20 000/200 000 (HEK293T:VeroE6)). To allow for sufficient fusion activity, the cells were left overnight at 37°C. Imaging was performed the next day with NIKON A1R (20x magnification) after fixation of the cells. Most representative picture is depicted.
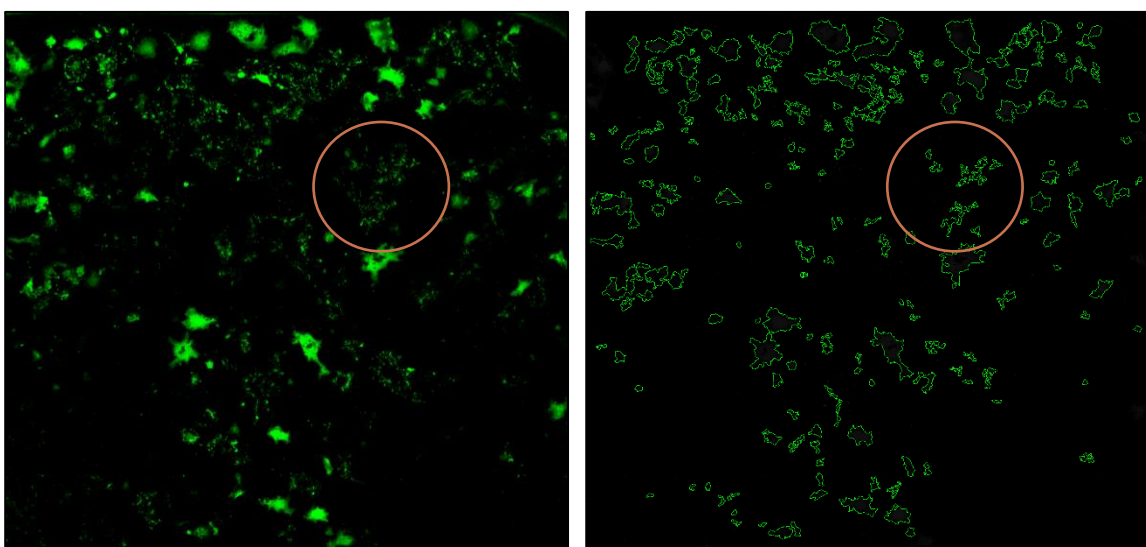
S2.5

Figure S2. 5 – Limitations of algorithmic syncytia identification. Syncytia that are not fully formed (e.g., red circle) cannot be accurately identified by the CellProfiler algorithm. Visualised by Nikon A1R microscopy (20x magnification)

33

Raw Data

Experiment	Data Type	Raw Data
Cell Ratio Assay	Olympus Images	Cell-Cell Ratios
	GraphPad Data	Cell-Cell Ratio Determination.pzfx
Ratio Inhibition Assay	Olympus Images	Cell Cell Ratio Inhibition
	GraphPad Data	Cell Cell Ratio + Ab.pzfx
Cell Number Determination (Coverslip)	Cell Profiler Output	Cell Number Determination (Coverslips)
	Nikon A1R/STORM Images	Cell Number Determination (Coverslips)
	R Markdown Script	SCRIPT_COVERSLIP_RATIOS.Rmd
Cell Number Determination (microslide)	Cell Profiler Output	Cell Number Determination (IBIDI)
	Nikon A1R/STORM Images	Cell Number Determination (IBIDI)
	R Markdown Script	SCRIPT_MICROSLIDE_RATIOS.Rmd
Area vs Nuclei	Cell Profiler Output	AreavsNuclei
	Nikon A1R/STORM Images	Area vs Nuclei
	R Markdown Script	SCRIPT_AREAVSNUCLEI.Rmd
	Nuclei Count (Excel)	AreavsNuclei Data.xlsx
Inhibition Assay	Cell Profiler Output	Inhibition Assay
	Nikon A1R/STORM Images	Inhibition Assay
	R Markdown Script	SCRIPT_INHIBITION.Rmd
Camostat Concentration Range	Cell Profiler Output	Camostat Concentration Range
	Nikon A1R/STORM Images	Camostat Concentration Range
	R Markdown Script	SCRIPT_CAMOSTAT_RANGE.Rmd
CISTIM + S1B3inL1 Assay	Cell Profiler Output	CISTIM Compounds + Peptide
	Nikon A1R/STORM Images	Compound Testing (CISTIM + peptide)
	R Markdown Script	SCRIPT_COMPOUND_TESTING.Rmd
CISTIM Concentration Range Assay	Cell Profiler Output	CISTIM Concentration Range
	Nikon A1R/STORM Images	CISTIM Compound Concentration Range
	R Markdown Script	SCRIPT_CISTIM_RANGE_V2.Rmd
S1B3inL1 Concentration Range	Cell Profiler Output	S1B3inL1 Concentration Range
	Nikon A1R/STORM Images	S1B3inL1 Concentration Range
	R Markdown Script	SCRIPT_PEPTIDE_RANGE.Rmd
Protocol CellProfiler	CellProfiler Input	PROTOCOL CELLPROLIFER SYNCYTIA COUNT.cpproj

All files can be found in the VIRshare